Tampere University

Elias Paakkunainen

COUPLED FINITE ELEMENT AND MICROMAGNETIC MODELING OF IRON LOSSES IN TAPE WOUND MAGNETIC CORES

ABSTRACT

Elias Paakkunainen: Coupled Finite Element and Micromagnetic Modeling of Iron Losses in Tape Wound Magnetic Cores
Master of Science Thesis
Tampere University
Master's Programme in Electrical Engineering
March 2022

A new model is developed to predict iron losses in tape wound magnetic cores. The model aims to accurately predict the losses at high excitation frequencies and take into account the geometry of tape wound cores better than already existing methods. There is a demand for accurate models of magnetic components at high frequencies, for example, due to the development of power electronics towards higher switching frequencies. The increased complexity of the developed model is expected to lead to longer simulation times.

Three different methods are utilized to study relevant phenomena. These include the models developed in this thesis: the 1D micromagnetic model with eddy currents (1DMMEC) and the coupled 1D micromagnetic – 2D FE model (1DMMEC–2DFE). Additionally, 3D micromagnetic simulations with MuMax3 are carried out. The iron losses are determined with all of these methods. Suitable numerical implementation of micromagnetic theory is also chosen. The 1DMMEC model introduces an approach where the tape material is modeled with micromagnetic theory, and the solution of the eddy current problem is approximated using a cosine series. The input to the model is the magnetic flux density, and the model is derived for a single strip of tape. The 1DMMEC–2DFE model is derived to consider better the cross-section geometry of tape wound cores. The model couples the 1DMMEC model to a 2D FEM formulation. The resulting model allows expanding the micromagnetic description of the tape material over the cross-section of tape wound cores.

The 3D micromagnetic simulations with MuMax3 cannot accurately model the iron losses. Direct simulation of the tape is not possible due to the computational burden, and small-scale simulations do not give satisfactory results. However, some magnetization processes in the tape can be examined through 3D micromagnetic simulations. The iron losses predicted with the 1DMMEC model are in good agreement with similar models from the literature. This motivates to attempt to couple the model with the 2D FEM to obtain a more general description of tape wound cores. The iron losses predicted with the 1DMMEC–2DFE model achieve good agreement with measured losses. In some situations, the predicted losses describe the measurements more accurately than the 1DMMEC model. The accuracy of the prediction seems to decrease slightly with thinner tape thicknesses. On the other hand, the simulation parameters were not varied to achieve the best fit to the measured losses in every situation. The computational burden of the 1DMMEC–2DFE model is significant with small excitation frequencies.

Keywords: eddy currents, finite element method, iron losses, micromagnetic theory, tape wound core

TIIVISTELMÄ

Elias Paakkunainen: Nauhasydämen rautahäviöiden mallintaminen mikromagnetiikan elementtimenetelmään kytkevällä mallilla
Diplomityö
Tampereen yliopisto
Sähkötekniikan DI-ohjelma
Maaliskuu 2022

Tässä diplomityössä kehitetään uusi menetelmä ohuesta nauhasta rullatun rautasydämen häviöiden laskemiseksi. Malli pyrkii ennustamaan tarkasti suuritaajuuksisten magneettikenttien aiheuttamat häviöt. Toisena tavoitteena on huomioida nauhasydämen muoto paremmin kuin mihin toistaiseksi kirjallisuudessa esitetyt mallit pystyvät. Esimerkiksi tehoelektroniikan kytkentätaajuuksien kasvaminen luo tarpeen tarkemmille magneettisten komponenttien malleille suurilla taajuuksilla. Kehitettävän mallin kasvavan monimutkaisuuden oletetaan lisäävän simulointiin kuluvaa aikaa.

Nauhasydämen mallinnukseen käytetään kolmea eri menetelmää. Käytettäviä menetelmiä ovat tässä työssä kehitettävät mallit: 1D mikromagnetiikka-pyörrevirtamalli (1DMMEC) ja 2D elementtimenetelmään kytketty 1D mikromagnetiikka-pyörrevirtamalli (1DMMEC–2DFE). Edellä mainittujen mallien lisäksi käytetään 3D mikromagneettisia simulointeja, jotka suoritetaan MuMax3-nimisellä ohjelmalla. Nauhasydämen rautahäviöt määritetään kaikilla kolmella lähestymistavalla. Työssä kehitettyjen mallien johtamiseen käytetään tilanteeseen soveltuvaa numeerista arviota mikromagnetiikasta. 1DMMEC-malli soveltaa mikromagneettista teoriaa nauhan materiaaliin, ja pyörrevirrat nauhan paksuuden yli ratkaistaan kosinisarjaa hyödyntävän approksimaation avulla. Mallin sisäänmenosuureena on magneettivuontiheys, ja malli on johdettu yksittäiselle, suoralle nauhan palalle. 1DMMEC–2DFE -malli pyrkii ottamaan nauhasydämen rakenteen paremmin huomioon. Kyseinen malli yhdistää 1DMMEC-mallin 2D-elementtimenetelmään. Yhdistetty malli mahdollistaa nauhasydämen poikkileikkauksen mallintamisen mikromagneettisen teorian avulla.

MuMax3-ohjelmalla tehtyjen mikromagneettisten 3D simulaatioiden avulla ei voida ennustaa nauhasydämen rautahäviöitä tarkasti. Riittävän suurta palaa nauhasta ei voida mallintaa suoraan 3D simulaatioiden avulla, koska kyseiset simulaatiot olisivat liian raskaita. Simuloitaessa pienempiä systeemejä lasketut häviöt eivät vastaa muilla menetelmillä määritettyjä häviöitä. Pienemmät systeemit soveltuvat kuitenkin nauhan magnetisaatiodynamiikan tutkimiseen. 1DMMEC-mallilla lasketut rautahäviöt vastaavat kirjallisuudessa esitettyjen mallien tuloksia. Tämä vahvistaa mallin toimivan oikein, ja se voidaan yhdistää 2D-elementtimenetelmään. 1DMMEC–2DFE -mallilla lasketut rautahäviöt vastaavat hyvin nauhasydänten mitattuja rautahäviöitä. Joissain tapauksissa yhdistetty malli on tarkempi kuin 1DMMEC-malli. Yhdistetyn mallin tarkkuus heikkenee, kun nauhasydämen nauhaa ohennetaan. Toisaalta simulaatioparametreja ei vaihdeltu eri simulaatioissa parhaan mahdollisen tuloksen saamiseksi. Laskenta 1DMMEC–2DFE -mallilla on matalilla taajuuksilla hidasta.

Avainsanat: elementtimenetelmä, mikromagnetiikka, nauhasydän, pyörrevirrat, rautahäviöt

PREFACE

This thesis was written while working in the research group of Electromechanics at Tampere University. I would like to thank my supervisors, Associate Professor Paavo Rasilo and Professor Lasse Laurson, for their guidance and interest in this project. Particularly, I wish to thank Associate Professor Paavo Rasilo for suggesting this interesting topic and offering the opportunity to work in the Electromechanics group.

Carrying out the simulations of this thesis required a lot of computing power, and the computational resources obtained from TCSC Narvi Cluster and Galerkin-PC are acknowledged. Special thanks go to Dr. Alexandre Halbach and Antero Marjamäki for maintaining the Galerkin-PC. Reda Elkhadrawy is thanked for numerous helpful discussions, as are the people of the Electromechanics group for all the coffee break discussions on- and off-topic.

Finally and most importantly, I want to thank my family and friends for the support I received during this thesis work and my studies.

Tampere, 11th March 2022

Elias Paakkunainen

CONTENTS

LIST OF SYMBOLS AND ABBREVIATIONS

$\boldsymbol{\alpha}$	vector of cosine functions in 1D cosine series model
α_{G}	LLG-equation damping parameter
α_n	cosine function in 1D cosine series model
γ_{G}	electron gyromagnetic ratio
Δt	timestep length
δ_{ij}	Kronecker delta
μ	permeability
μ_0	permeability of free space
ν	reluctivity
ν_0	reluctivity of free space
Ω	domain of a 2D finite element problem
ϕ	rotation angle
σ	electric conductivity

$\boldsymbol{A}$	magnetic vector potential
A_{ex}	exchange stiffness constant
$\boldsymbol{a}$	magnetic vector potential nodal values
a	variable of 1D micromagnetic model with eddy currents
$\boldsymbol{B}$	magnetic flux density
$\boldsymbol{B}_{\mathrm{eff}}$	effective magnetic flux density
B_{max}	amplitude of sinusoidal magnetic flux density
B_{rad}	radial component of magnetic flux density
B_{tan}	tangential component of magnetic flux density
$\boldsymbol{b}$	vector containing magnetic flux density coefficients
b	magnetic flux density in 1D considerations
b_n	magnetic flux density coefficient in 1D cosine series model

$\boldsymbol{C}$	matrix of 1D cosine series model
c	variable of 1D micromagnetic model with eddy currents
$\boldsymbol{D}$	2D discrete curl operator
d	tape thickness
$\hat{\boldsymbol{e}}$	unit vector
$\boldsymbol{F}$	vector of coupled 1D micromagnetic – 2D FE model
f	frequency
$\boldsymbol{G}$	matrix of coupled 1D micromagnetic – 2D FE model
$\boldsymbol{H}$	magnetic field strength
$\boldsymbol{H}_{\mathrm{a}}$	applied magnetic field strength
$\boldsymbol{H}_{\mathrm{an}}$	anisotropy field strength
$\boldsymbol{H}_{\mathrm{eddy}}$	eddy current field strength
$\boldsymbol{H}_{\mathrm{eff}}$	effective magnetic field strength
$\boldsymbol{H}_{\mathrm{ex}}$	exchange field strength
$\boldsymbol{H}_{\mathrm{ms}}$	magnetostatic (demagnetizing) field strength
$\boldsymbol{H}_{\mathrm{s}}$	matrix containing 2D magnetic field strength at surface of the tape
H_{rad}	radial component of magnetic field strength
H_{tan}	tangential component of magnetic field strength
$\boldsymbol{h}_{\mathrm{s}}$	vector containing magnetic field strength at surface of the tape
h	magnetic field strength in 1D considerations
h_{s}	magnetic field strength at surface of the tape
$\boldsymbol{I}$	identity matrix
$\boldsymbol{i}$	conductor currents
$\boldsymbol{J}$	Jacobian matrix
K_{u}	anisotropy constant
$\boldsymbol{M}$	magnetization
M_{s}	saturation magnetization
$\boldsymbol{m}$	relative magnetization
$\boldsymbol{N}$	geometry dependent matrix in magnetostatic field calculation
N	number of domains
N_{b}	number of terms in the cosine series
N_{cell}	number of discretization cells

N_p	number of nodal points in 2D mesh
p	volumetric power (loss) density
p_cl	classical contribution in loss separation
p_dw	domain wall contribution in loss separation
p_ex	excess loss contribution in loss separation
p_hy	hysteresis contribution in loss separation
p_sd	spin damping contribution in loss separation
$\boldsymbol{R}$	rotation matrix
$\boldsymbol{r}$	residual vector
T	time period
t	time variable
$\boldsymbol{u}$	conductor voltages
u	coordinate axis of 1D micromagnetic model with eddy currents
$\boldsymbol{V}$	matrix of 1D micromagnetic model with eddy currents
V_cell	discretization cell volume
v	coordinate axis of 1D micromagnetic model with eddy currents
$\boldsymbol{W}$	vector containing shape functions
W_i	shape function
w	coordinate axis of 1D micromagnetic model with eddy currents
$\boldsymbol{x}$	solved variable in Newton-Raphson iteration

1DMMEC	1D micromagnetic model with eddy currents
1DMMEC–2DFE	coupled 1D micromagnetic – 2D FE model
DW	domain wall
FE	finite element
FEA	finite element analysis
FEM	finite element method
LLG	Landau-Lifshitz-Gilbert (equation)
PBC	periodic boundary condition
PDE	partial differential equation

1 INTRODUCTION

There is a constant demand for new modeling techniques to push further the frontier of what is accessible through computer simulations. The demand stems from both academia and the industry. Novel modeling techniques are a subject of research as themselves, and they may help reduce the amount of costly and time-consuming prototyping in the industry. The subject of interest is not only to be able to model bigger and more complex systems but also to, sometimes only roughly, replicate results with a lower computational burden.

The system examined in this thesis is a tape wound magnetic core. Tape wound cores are often one alternative for the core topology of toroidal inductors. Of particular interest are the power losses in the core when it is subjected to varying magnetic fields. Generally, these losses are referred to as iron losses. Recent pursuits for energy efficiency and more compact magnetic components motivate studies of loss mechanisms and more accurate models.

Using conventional methods to model the iron losses in tape wound cores gives satisfactory results at low excitation frequencies, but the accuracy reduces at high frequencies. This is problematic, for example, due to the development of power electronics towards higher frequencies through new switch devices [1]. There exist models utilizing micromagnetic theory, which improve the accuracy of estimated losses in the high-frequency range [2, 3]. However, these models are developed for a single strip of tape instead of an entire tape wound core.

The aim of this thesis is to create a model for tape wound magnetic cores that couples the 2D finite element (FE) method (FEM) and micromagnetic theory. The model is expected to be able to take into account the geometry of tape wound cores and utilize micromagnetic theory in a system conventionally considered too large for micromagnetic description. The research question is to study the accuracy of the created model compared to measured results and existing methods. The quantity of primary interest is the predicted iron losses of the core. Additionally, attention is paid to the computational performance of the model.

The outline of this thesis is the following. Chapter 2 presents general concepts in magnetic materials and iron loss modeling. In Chapter 3, the emphasis is on tape wound cores. Their materials and applications are presented, and general magnetic properties

are described in more detail for tape wound cores. Chapter 4 presents the mathematical modeling that was done in this work. The used formulations of the micromagnetic theory and FEM are also introduced. Chapter 5 presents the results that were obtained with the methods described in Chapter 4. The results are compared to models presented in the literature, and their properties are discussed. Chapter 6 sums up the most important results and observations of this work. Additionally, suggestions are made for future work on the topic.
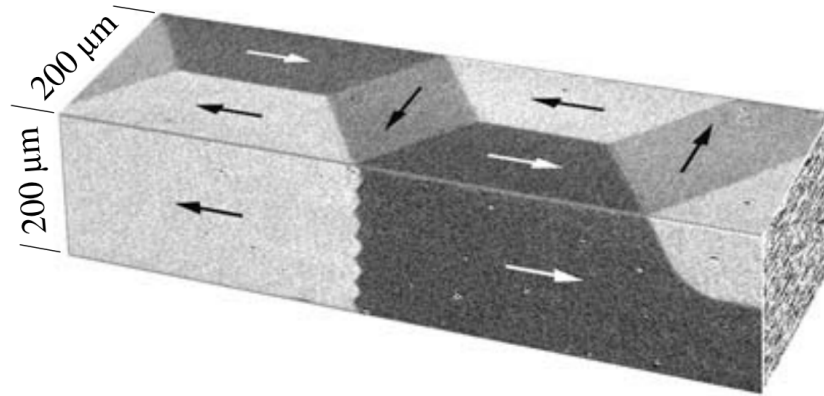
2 MAGNETIC MATERIALS

This chapter introduces some important concepts of magnetism in matter at a general level. First, magnetism is discussed on a microscopic scale. The second part of this chapter concentrates on a macroscopic approach to magnetism and discusses power dissipation in magnetic materials.

2.1 Magnetic domains and domain walls

When observing the magnetic properties of a material on a microscopic scale, the relevant quantity is the magnetization M which describes the magnetic state of the body. A classical description can be obtained by postulating elementary magnetic moments in magnetized matter. These magnetic moments can be thought to behave similarly to magnetic moments of individual atoms. The magnetization field in the matter is the volume average of the contributions of the elementary magnetic moments. The magnetization is continuous and smooth over the volume of the body. [4]

Generally, macroscopic bodies of magnetic material consist of magnetic domains and domain walls (DW). Separate domains are identified by the different orientations of M. Inside domains, the magnetization is assumed to be approximately uniform, i.e., pointing to the same direction at every point. Although originally the existence of domains was solely theorized, these days direct observation is possible. Figure 2.1 shows an example of observed magnetic domains in iron.

DWs are the regions separating two different domains. In a DW, the magnetization of one domain smoothly changes to the magnetization of the neighboring domain. DWs can be divided into Bloch and Néel types depending on how the magnetization changes from one domain to another in the 3D space. Also, such DWs exist that cannot be put to either of these categories. Additionally, DWs can be characterized by the change in orientation of M between neighboring domains to, for example, 180° or 90° DWs. Despite taking only a small fraction of the volume of the body, DWs contribute significantly to the magnetization dynamics. The effects of the motion of DWs and possible interplay with the structural disorder are also often observable on the macroscopic scale. The interaction of structural defects and DWs is known as wall pinning.

Figure 2.1. *Domains in iron observed with magneto-optical methods. Observations from two surfaces of the sample have been combined to create a 3D appearance. [5]*

Domains and DWs exist in magnetic materials because it is energetically favorable. The driving force behind the formation of these patterns is the pursuit to minimize the energy of the system, which is dependent on different contributions and phenomena. Factors contributing to the energy of the system are presented in Chapter 4 alongside introducing micromagnetic theory. Going further, these phenomena have different dependencies of the situation to be examined, resulting in the statement that the magnetization of the body is above all case dependent. For example, the question whether this subdivision to domains and DWs even happens depends on the size of the body examined. In small bodies, the magnetization tends to be uniform, whereas with larger systems often separate domains appear. [4, 5]

2.2 Magnetization process and iron loss mechanisms

When the power losses due to a change in the magnetic state of magnetic material are to be determined, the material response to the given excitation has to be known. The physical origin of this power dissipation is the irreversible processes that occur when the elementary magnetic moments in the material change their orientation. These losses are often referred to as iron losses. In practice knowing the material response means simultaneously knowing the time evolution of the magnetic flux density B and magnetic field strength H in the material. This can be determined with the material property, or constitutive relation, of the system. The material property is often presented as $B(H)$, implying that B can be determined when H is known.

In the following, different possibilities for the $B(H)$ relation are discussed alongside their properties. The most straightforward approach is to assume a linear dependency be-

tween the fields

$$B = \mu H, \qquad (2.1)$$

where μ is the material permeability. The inverse of μ is called the material reluctivity ν. The accuracy of (2.1) can be improved by replacing the constant μ with a magnetic flux density dependent permeability $\mu(\|B\|)$. Despite being simplified descriptions of the actual material behavior, both of the mentioned single-valued permeabilities have their region of validity. Constant permeability refers to magnetically linear material and can be useful with small fields and non-ferromagnetic materials. With big fields, however, this approach is not feasible because it neglects magnetic saturation altogether, which can be taken into account by using $\mu(\|B\|)$. Neither of these approaches is hysteretic, and thus they cannot predict a hysteresis loop. [6]

In general, the behavior of magnetic materials is hysteretic. With much simplification, magnetic hysteresis can be seen as a phenomenon in which the instantaneous B is not merely a function of the instantaneous H but also depends on other factors. Above all, the history of the former excitation field values and magnetic states of the system is significant. A typical example of hysteretic behavior is the hysteresis loop: when H is increased from an initial value to a certain magnitude and then back to the initial value, $B(H)$ does not return towards its initial value along the same path and is not even guaranteed to reach this value. The traces of B with respect to H are referred as hysteresis loops or alternatively $B(H)$-loops. The area of a closed hysteresis loop corresponds to the energy dissipated during the cycle. Figure 2.2 shows a conceptual representation of a few different possible hysteresis loops. [4]

The hysteresis loops also provide an example of phenomena originating from the magnetic microstructure being observable in macroscopic samples. A closer examination of the traces of B with respect to H reveals that the trace is not smooth but instead behaves in a step-wise manner. These abrupt changes are referred to as *Barkhausen jumps*. They can be explained in terms of the changing energy landscape of the system as an external field is imposed. As the system attempts to minimize its energy, consecutive jumps to new local energy minima occur, and M changes accordingly. It needs to be noted that the global minimum of energy is rarely obtained due to the higher energy values separating two minima.

More generally, B can be expressed as a function of both H and M

$$B = \mu_0(H + M), \qquad (2.2)$$

where μ_0 is the permeability of free space. The complication of this added generality is
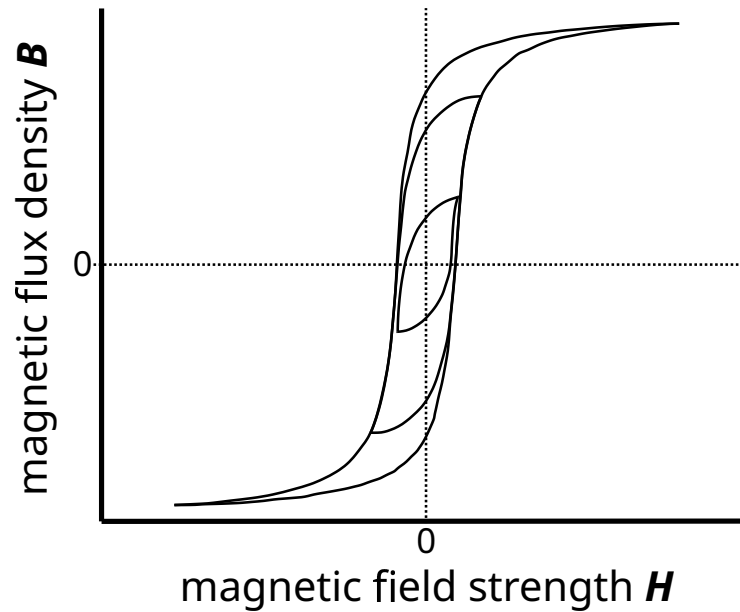
Figure 2.2. *Conceptual illustration of hysteresis loops. Two minor loops are depicted alongside the main loop, which reaches magnetic saturation. Quantities B and H are used on the axes despite being vector fields. In order to plot $B(H)$-loops, the fields have to be expressed with a single value. This can be achieved, for example, through spatial averages.*

that now also M has to be determined. Predicting M in macroscopic bodies of magnetic material is difficult. In this work, the Landau-Lifschitz-Gilbert (LLG) equation will be used to determine M. The LLG equation and the methods used to evaluate it will be introduced in Chapter 4.

When determining the iron losses in magnetic materials, the concept of *loss separation* is often used. Loss separation means that the total iron losses can be divided to separate loss contributions which can be calculated independently. Using loss separation, the volumetric power loss density p can be expressed as

$$p = p_{\text{cl}} + p_{\text{hy}} + p_{\text{ex}}. \tag{2.3}$$

To introduce the contributions briefly, classical losses p_{cl} are the eddy current losses that can be calculated from Maxwell's equations for a macroscopically homogeneous medium. The hysteresis losses p_{hy} originate from the intrinsic rate-independent magnetization processes on the fine scale. The excess losses p_{ex} account for the intrinsic rate-dependent processes. Being hard to model, p_{ex} is sometimes simply considered as the difference between the measured losses and the sum of p_{cl} and p_{hy}. [4]

Throughout this thesis, the losses will be expressed as volumetric loss densities. The calculation of total power loss can be carried out by integrating p over the volume of the magnetic material.

3 TAPE WOUND MAGNETIC CORES

In this chapter, the theoretical background presented in Chapter 2 is applied to tape wound magnetic cores. Tape wound cores are presented with some examples of applications. Additionally, the magnetic domain structure of the tape material and the chosen approach to loss modeling are discussed.

3.1 Applications

A tape wound magnetic core is constructed by winding a thin tape into a spiral structure. Separate layers of the core are insulated from each other. An inductor with a tape wound core can, in principle, be used anywhere where a magnetic component is required. However, for practical reasons, they prove to be the optimal choice in specific applications. Figure 3.1 shows an example of a commercial tape wound core.

The magnetic properties of the tape wound core originate directly from the core material and dictate the suitable application. From the perspective of core losses, the two most attractive materials are Co-based *amorphous* alloys and *nanocrystalline* alloys. Co-based alloys are the example case for which ultimately the losses will be modeled in this work. To be more specific, $Co_{71}Fe_4B_{15}Si_{10}$ and $Co_{67}Fe_4B_{14.5}Si_{14.5}$ will be examined. Nanocrystalline alloys consist of Fe-Cu-Nb-Si-B, and they are also known by tradenames FINEMET and VITROPERM. The performance of these materials in terms of losses is roughly speaking similar. [8, 9]

When comparing the magnetic performance of Co-based amorphous and nanocrystalline alloys to more conventional materials, the differences become clearer. These materials perform better than permalloy (Ni-Fe alloy), ferrites, or laminated steels. The usage of laminated steels is not efficient with frequencies significantly higher than line frequency. Also, tape wound cores are not manufactured from ferrites, but they are still mentioned here due to their extensive use as a core material. Ferrite cores are often solid due to the low conductivity of ferrites. The superior performance over a wide range of frequencies compared to the ferrite cores makes Co-based and nanocrystalline tape wound cores an attractive alternative for some applications. Better magnetic properties of the tape wound core allow reduction of size and weight of magnetic components. Lower core losses improve efficiency. [8, 10]

Figure 3.1. *Commercial tape wound core and its casing. The picture is taken from the website of a retailer [7].*

The applications of Co-based and nanocrystalline tape wound cores require high efficiency and compact system size. Often, the device operates with high frequency, but also line frequency applications exist, such as earth leakage circuit breakers and electronic energy meters. With higher frequencies, multiple possible applications are available in the different inductors required for switched-mode power supplies. For example, these include power transformers, common mode chokes, storage chokes, and magnetic amplifiers. Additional examples of applications exist in telecommunication and automotive electronics. [11]

To conclude the practical discussion on tape wound cores, Figure 3.2 presents a schematic of the core cross-section. The schematic exaggerates the layered structure of the core for demonstration purposes. Also, the coordinate system over the core geometry is defined and will be used throughout the rest of this thesis. Along with the standard Cartesian coordinates, radial and tangential components will be utilized. Angle ϕ is defined as the angle between an arbitrary position vector and the x-axis.

3.2 Domain structure

Figure 3.3 illustrates the assumed domain structure in the tape of the tape wound core in this work. A separate Cartesian coordinate system with axes denoted as u, v, and w is used on the scale of a few domains of the tape. The structure is assumed to be very regular, with the magnetizations of neighboring domains pointing in the opposite directions along the axis dictated by material anisotropy. Anisotropy refers to an intrinsic property of the material, which makes it more favorable for the material to be magnetized in specific directions. Anisotropy will be discussed in more detail in Chapter 4. Also, for
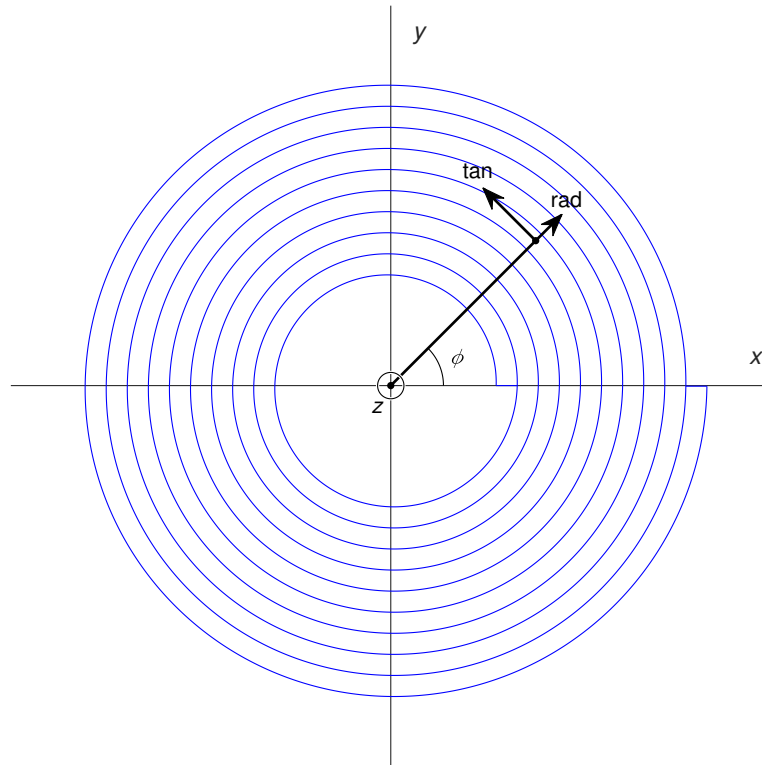
Figure 3.2. *Illustration of the cross-section of the tape wound core geometry. Additionally, the coordinate system used in this work is presented.*

simplicity, the domain width is assumed to be constant in the tape.

The external field affecting the material is applied perpendicular to the direction of the anisotropy axis, in the direction of v-axis in the coordinate system of Figure 3.3. Under the sinusoidally varying external field, the magnetizations of the domains are expected to oscillate around the anisotropy axis. However, the deviations from the initial positions are assumed to be small. Particular emphasis needs to be given that the only expected response to the external field is the rotation of the domain magnetizations. Consequently, many more general magnetization phenomena are neglected, such as changes in domain volumes and positions as well as processes including the DWs. In fact, the effects of DWs are neglected in this work. With these assumptions it is enough to model the dynamic magnetization over the tape thickness $w \in \left[-\frac{d}{2}, \frac{d}{2}\right]$ in only one point (u, v) of the tape plane in order to obtain the dynamic magnetization of the whole tape. The thickness of the tape is denoted with d.

The long list of assumptions in the previous paragraphs can only lead to the conclusion that the domain structure assumed in this work is very idealized and cannot be valid in general situations. With this simplified scheme, it has to be accepted that some, not necessarily negligible, phenomena are neglected. Two important aspects will be discussed further: whether such a simple and regular domain structure can exist in real materials and whether the DW processes can be ignored.
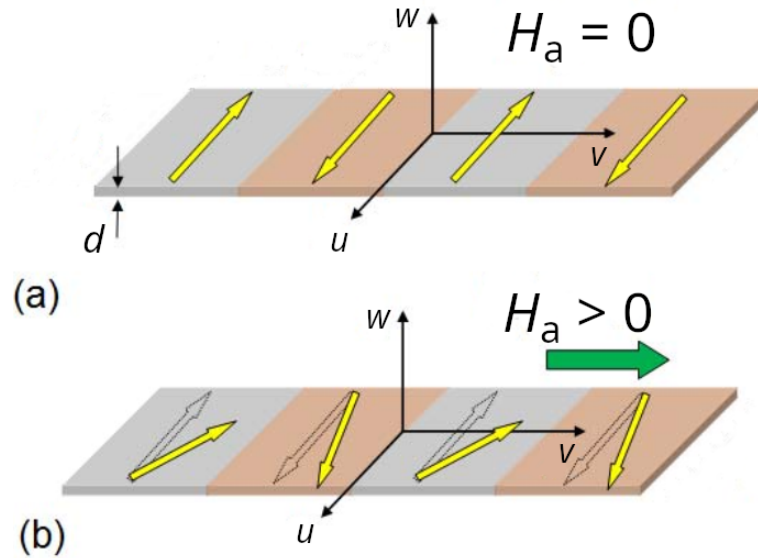
Figure 3.3. *Assumed domain structure of the tape. The arrows show the orientation of the magnetization in the domains. (**a**) Without applied magnetic field strength, (**b**) with applied magnetic field strength in the v-direction. Image modified from [2].*

The first notion that needs to be made is that for such a regular antiparallel domain pattern to exist, the tape must be very thin, and a large enough anisotropy must be present in the material. Otherwise, it would not be energetically favorable for all the domain magnetizations to point in the direction of the anisotropy axis. Secondly, the magnetization of the body has a complex dependency of material parameters and previous states of the system [4]. Particularly this history dependency is utilized when the desired state of the sample is obtained through annealing, i.e., through suitable treatment of high temperature and external magnetic field. In literature, there are examples where the required anisotropy and desired domain structure are obtained in thin tapes through annealing [12, 13].

The important aspect of DWs is whether they move due to the varying external field. DW motion is considered a separate loss mechanism, which the model developed in this work does not take into account. In the presented domain structure, the DW motion decreases as a function of external field frequency [14]. As the motion decreases with high frequencies, it can ultimately be neglected. This can be assumed to happen in the megahertz range with the materials examined in this work. The relaxation of DW motion has been experimentally shown through Kerr microscopy. [14, 15]

3.3 Loss separation

In this work, it is advantageous to write (2.3) as

$$p = p_{\mathrm{cl}} + p_{\mathrm{sd}} + p_{\mathrm{dw}}, \tag{3.1}$$

where the introduced contributions p_{sd} and p_{dw} contain the sum of p_{hy} and p_{ex} divided differently. In (3.1), p_{sd} denotes the loss contribution originating from so-called spin damping, and p_{dw} losses from DW processes. There exist formulae to calculate both p_{hy} and p_{ex} but they, in particular p_{ex}, are quite phenomenological with dependencies from intrinsic processes hard to quantify. These formulae will not be presented. According to the considerations in the previous section, p_{dw} can be neglected at high frequencies, and thus the total losses are assumed to be the sum of p_{cl} and p_{sd}.

In the following, different ways to calculate p_{cl} are briefly discussed. The motivation for this is to show that these approaches, often used as the standard solutions to estimate the losses, are not applicable to the application of this work. Apart from the fact that estimating the total losses with p_{cl} neglects p_{sd}, there are also other factors affecting the accuracy of this approximation. The different methods to calculate p_{cl} usually give different results depending on the used material property. An exception to this rule worth mentioning is the well-known low-frequency limit equation

$$p_{\mathrm{cl}} = \frac{\pi^2}{6}\sigma d^2 B_{\mathrm{max}}^2 f^2, \tag{3.2}$$

where B_{max} and f are the amplitude and frequency of the sinusoidal magnetic induction. The electric conductivity of the material is denoted with σ. The remarkable thing about this equation is that the classical losses can be predicted without knowing the material property at low frequencies. However, the frequencies of interest in this work are too high for this equation to be used.

The generalized version of (3.2) derived for linear material property is

$$p_{\mathrm{cl}} = \frac{\pi}{2}\frac{\gamma B_{\mathrm{max}}^2 f}{\mu}\frac{\sinh\gamma - \sin\gamma}{\cosh\gamma - \cos\gamma}, \tag{3.3}$$

where $\gamma = \sqrt{\pi\sigma\mu d^2 f}$ [4]. The used material property is present in the formulation through the presence of μ in the equation. Even though (3.3) is derived assuming a linear material property and the material property used in this work will be the LLG equation, the sum of classical and spin damping losses could, in theory, be determined with this equation. In order to do so, $\mu(f)$ would have to be solved from the changed material property. In [16], a measured $\mu(f)$ is used alongside (3.3) to predict the losses in a tape

wound ring at high frequencies, and a good agreement with measurements is achieved. However, the losses will ultimately be calculated from the field quantities because defining the lumped parameter μ in each situation is unnecessary.

If (3.3) would be used with the linear material property, the resulting losses in high frequencies would be greatly underestimated when compared to the measured losses. At high frequencies, a linear $B(H)$ relationship predicts the loss per cycle to be proportional to $f^{1/2}$ whereas the proportionality according to the measurements is approximately f [2]. This difference is due to the coupling of eddy currents and spin dynamics, which is not taken into account with the linear material property. In other words, the contribution of p_{sd} is neglected. By using the LLG equation in the constitutive law, this phenomenon is taken into account, and the high-frequency power loss calculation becomes more accurate [3].

In what follows, the field quantities are denoted with b and h to distinct the fields over the tape thickness from the corresponding macroscale quantities. The focus is on thin layers of tape in which the thickness of the tape is small compared to the other dimensions. This allows us to model the situation in 1D and consider the fields b and h as scalar quantities facing in the direction parallel to the surface of the tape. The losses containing both eddy current and spin damping contributions can be expressed as

$$p_{\mathrm{cl}} + p_{\mathrm{sd}} = \frac{1}{T} \int_T h_{\mathrm{s}}(t) \frac{db_0(t)}{dt} dt \tag{3.4}$$

where h_{s} is the magnetic field strength on the surface of the tape and b_0 the average magnetic flux density in the tape [17]. The time variable is denoted with t, and T is the period. The time-averaged losses are presented here to express the losses in comparable form to (3.2) and (3.3). Equation (3.4) allows determining the losses directly from the field quantities without defining μ. Expressing the losses using these quantities is beneficial in experimental measurements and, as will be seen, in the chosen modeling approach.

To complete the discussion on loss modeling, a method to obtain $b(w, t)$ and $h(w, t)$ is presented. The coordinate along the thickness of the tape is denoted with w. In practice, the fields are obtained by solving an eddy current problem over the thickness of the tape. When b and h are scalar fields in a thin layer of tape, the eddy current problem can be solved by solving a 1D diffusion equation [18]

$$\frac{\partial^2 h(w, t)}{\partial w^2} = \sigma \frac{\partial b(w, t)}{\partial t}. \tag{3.5}$$

In this work, solution of (3.5) is approximated with a model presented in [18]. The main idea of the model to be presented is to express $b(w, t)$ and $h(w, t)$ with truncated cosine series. The cosine series allows to express $b(w, t)$ as a linear combination of coefficients $b_n(t)$ and cosine functions $\alpha_n(w)$ which are defined as $\alpha_n(w) = \cos(2n\pi \frac{w}{d})$. With these
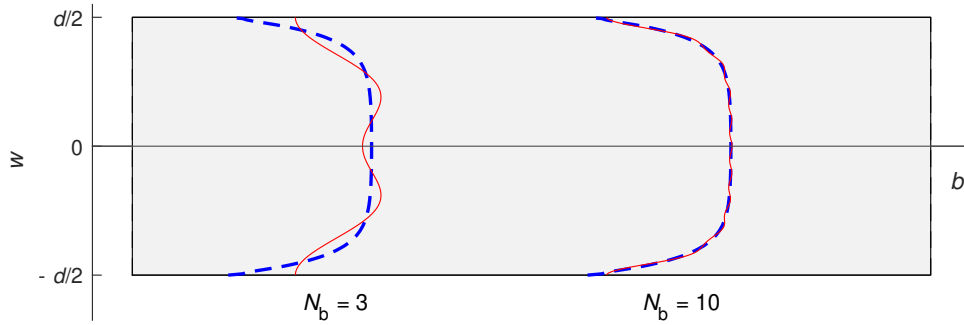
Figure 3.4. *Illustration of the approximation of $b(w,t)$ with a cosine series. The blue dashed lines are the profile of $b(w)$ towards which the cosine series converges. The red lines give two examples of the estimated profiles with relatively small N_{b}. As N_{b} is increased, the accuracy of the approximation increases.*

definitions, $b(w,t)$ can be expressed as

$$b(w,t) = \sum_{n=0}^{N_{\mathrm{b}}-1} b_n(t)\alpha_n(w), \tag{3.6}$$

where N_{b} is the number of cosine terms in the cosine series. Figure (3.4) shows how the cosine series approximation of $b(w,t)$ converges as N_{b} is increased. The magnetic field strength at the surface of the tape can be calculated from

$$\underbrace{\begin{bmatrix} h_{\mathrm{s}}(t) \\ 0 \\ \vdots \\ 0 \end{bmatrix}}_{\boldsymbol{h}_{\mathrm{s}}} = \frac{1}{d}\int_{-d/2}^{d/2} \underbrace{\begin{bmatrix} \alpha_0(w) \\ \alpha_1(w) \\ \vdots \\ \alpha_{N_{\mathrm{b}}-1}(w) \end{bmatrix}}_{\boldsymbol{\alpha}} h(b(w,t))dw + \sigma d^2 \boldsymbol{C}\frac{\partial}{\partial t} \underbrace{\begin{bmatrix} b_0(t) \\ b_1(t) \\ \vdots \\ b_{N_{\mathrm{b}}-1}(t) \end{bmatrix}}_{\boldsymbol{b}}, \tag{3.7}$$

where $h(b(w,t))$ is the material property. Until now, the material property has always been presented as $\boldsymbol{B}(\boldsymbol{H})$ but the definition of $\boldsymbol{H}(\boldsymbol{B})$ is equally possible. The matrix $\boldsymbol{C}$ is a constant matrix with the dimensions of $N_{\mathrm{b}} \times N_{\mathrm{b}}$. The method to evaluate $\boldsymbol{C}$ is presented in [18]. Equation (3.7) defines the abbreviations that will be used later in this work for the vectors present in the equation. The column vector containing h_{s} is denoted as $\boldsymbol{h}_{\mathrm{s}}$, the used cosine functions as $\boldsymbol{\alpha}$ and the cosine series coefficients as $\boldsymbol{b}$.

In (3.7) as many terms in the series as necessary can be included by increasing N_{b}. Apart from the first value, all other entries of $\boldsymbol{h}_{\mathrm{s}}$ are 0. The input to (3.7) is either h_{s} or b_0, from which the other possible input variable and the higher-order magnetic flux density coefficients can be solved. In this work, b_0, which corresponds to the average magnetic

flux density in the tape, is the input for the model. When h_s is solved from (3.7), the loss in the tape material can be calculated by using (3.4).

4 METHODS FOR MODELING OF IRON LOSSES IN TAPE WOUND MAGNETIC CORES

This chapter presents three different approaches to model the iron losses in tape wound magnetic cores. The presented methods are referred to as 3D micromagnetic simulations, the 1D micromagnetic model with eddy currents (1DMMEC), and the coupled 1D micromagnetic – 2D FE model (1DMMEC-2DFE). Additionally, the used implementations of micromagnetic theory and FEM are presented.

4.1 3D micromagnetic simulations

In this section, the micromagnetic theory is briefly introduced. The concepts are presented in general terms, but the emphasis is on the numerical implementations used in this work which allow us to perform computations. Additionally, determining the losses by using 3D micromagnetic simulations is discussed.

Returning to the considerations in Chapter 2, the $B(\boldsymbol{H})$-relation of the material is known according to (2.2), when both $\boldsymbol{H}$ and $\boldsymbol{M}$ are known. Micromagnetic theory will provide the means to approximate $\boldsymbol{M}$.

4.1.1 Landau-Lifshitz-Gilbert equation

Micromagnetics is a theory that describes magnetism in a length scale between macroscopic Maxwell's equations and quantum mechanical descriptions of systems of atoms. In a way, micromagnetics combines these two theories by introducing some phenomena of quantum mechanical origin to an otherwise classical description. Micromagnetics is a continuum theory, meaning that the observed spatial scale is large enough to neglect atom level fluctuations in the field quantities. The theory is capable of approximating $\boldsymbol{M}$ in the volume of the system by attempting to minimize the total energy. The energy of the system is a sum of different contributions originating from different phenomena. The theory of micromagnetics was originally presented by Brown [19]. [20]

One of the core equations of micromagnetics is the Landau-Lifshitz-Gilbert equation

$$\frac{\partial \boldsymbol{M}}{\partial t} = -\frac{|\gamma_{\mathrm{G}}|\,\mu_0}{1+\alpha_{\mathrm{G}}^2}\boldsymbol{M}\times\boldsymbol{H}_{\mathrm{eff}} - \frac{|\gamma_{\mathrm{G}}|\,\mu_0}{1+\alpha_{\mathrm{G}}^2}\frac{\alpha_{\mathrm{G}}}{M_{\mathrm{s}}}\boldsymbol{M}\times(\boldsymbol{M}\times\boldsymbol{H}_{\mathrm{eff}}) \qquad (4.1)$$

which can be used to obtain the dynamical magnetization, i.e., the time evolution of $\boldsymbol{M}$. There exist several mathematically identical versions of the LLG equation. The equation is constrained with $\|\boldsymbol{M}\| = M_{\mathrm{s}}$, meaning that the amplitude of the magnetization is fixed and the only possible change is in the orientation. In (4.1), M_{s} is a material-dependent constant called the saturation magnetization, γ_{G} the electron gyromagnetic ratio, and α_{G} the phenomenological LLG equation damping parameter (also known as the Gilbert damping constant). The effective magnetic field strength $\boldsymbol{H}_{\mathrm{eff}}$ takes into account the different phenomena included in the micromagnetic total energy. In this work, $\boldsymbol{H}_{\mathrm{eff}}$ is expressed as

$$\boldsymbol{H}_{\mathrm{eff}} = \boldsymbol{H}_{\mathrm{ex}} + \boldsymbol{H}_{\mathrm{an}} + \boldsymbol{H}_{\mathrm{ms}} + \boldsymbol{H}_{\mathrm{a}} + \boldsymbol{H}_{\mathrm{eddy}} \qquad (4.2)$$

meaning that the magnetic field strength contributions of exchange interaction ($\boldsymbol{H}_{\mathrm{ex}}$), material anisotropy ($\boldsymbol{H}_{\mathrm{an}}$), magnetostatic field strength ($\boldsymbol{H}_{\mathrm{ms}}$), applied magnetic field strength ($\boldsymbol{H}_{\mathrm{a}}$), and the field strength caused by the eddy currents induced to the body ($\boldsymbol{H}_{\mathrm{eddy}}$) are taken into account. These phenomena are discussed in more detail in the next section. [21]

A visual interpretation of the LLG equation is presented in Figure 4.1. The equation describes a gradual evolution that results in $\boldsymbol{M}$ and $\boldsymbol{H}_{\mathrm{eff}}$ ultimately pointing in the same direction if $\boldsymbol{H}_{\mathrm{eff}}$ is kept constant long enough. A physical meaning can be given to both terms on the right side of the phenomenological LLG equation. The term proportional to $\boldsymbol{M}\times\boldsymbol{H}_{\mathrm{eff}}$ is the classical description of a rotational movement of $\boldsymbol{M}$ around $\boldsymbol{H}_{\mathrm{eff}}$. The second term proportional to $\boldsymbol{M}\times(\boldsymbol{M}\times\boldsymbol{H}_{\mathrm{eff}})$ is responsible for the damping of the motion, meaning that the sum of these terms is a description of damping precessional rotation. The strength of the damping is controlled by α_{G}. [20]

4.1.2 Effective magnetic field strength contributions

The different field contributions that are taken into account in evaluating $\boldsymbol{H}_{\mathrm{eff}}$ in this work were already presented in (4.2). In the following, these field contributions are introduced one by one. It should briefly be remarked that in this description, some phenomena affecting the magnetization $\boldsymbol{M}$ are neglected. For example, effects arising from magnetoelastic and thermal origins are neglected. It needs to be emphasized that the assumption to neglect structural disorder altogether is significant because, generally, the structural disorder is essential in the magnetization processes of bulk materials.
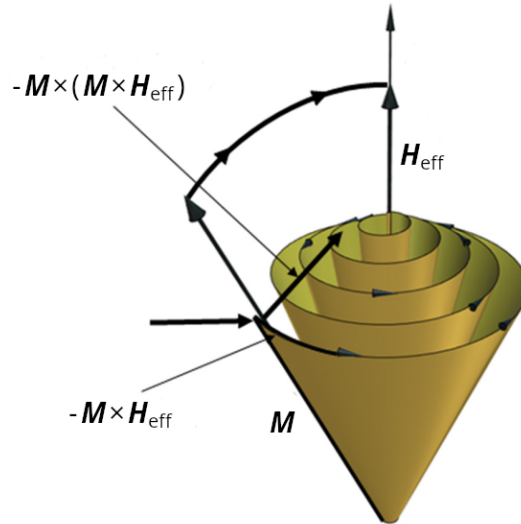
Figure 4.1. *Illustration of the LLG equation dynamics. The equation can be interpreted as a description of a damping precessional time evolution of M towards H_{eff}. Image modified from [22].*

Exchange field

The exchange field is due to the atomic scale exchange interaction, which attempts to keep neighboring magnetic moments pointing in the same direction. The physical origin of this quantum mechanical interaction is the coupling of separate electron orbitals and the requirement to satisfy the *Pauli exclusion principle*. This results in it being energetically favorable for macroscopic regions of the material to be uniformly magnetized in the same direction. [4]

In the case to be modeled, the exchange field H_{ex} over the thickness of the tape can be expressed as

$$H_{\text{ex}} = \frac{2A_{\text{ex}}}{\mu_0 M_{\text{s}}^2} \nabla^2 M, \tag{4.3}$$

where A_{ex} is the exchange stiffness constant, a material dependent parameter describing the strength of exchange interaction [2]. ∇^2 is the *Laplace operator* which can also be written as $\nabla^2 = \nabla \cdot \nabla$.

Attention needs to be paid to the numerical evaluation of the Laplace operator, i.e., the numerical evaluation of the second-order spatial derivatives of M. In this work, H_{ex} is evaluated by using the so-called 6 neighbor approximation, meaning that only the contribution of the closest 6 elements is taken into account in the calculation. In this context, elements refer to the cells of a finite difference mesh in which the cell size is determined by the spatial discretization in the direction of the thickness of the tape. When the assumed domain structure of Figure 3.3 is examined, the approximation reduces automatically to

take into account only 2 of the neighboring elements. In the plane perpendicular to the tape thickness, M is constant in the domains, and the spatial (numerical) derivatives are zero. The second-order derivative of M in the direction of the tape thickness is calculated by using the value of M in the element for which the calculation is carried out, and the values of M in the two neighboring elements along the thickness. Neumann boundary conditions are used on the surfaces of the tape. [23]

Anisotropy field

The anisotropy field $\boldsymbol{H}_{\mathrm{an}}$ also originates from quantum mechanical considerations. For anisotropic materials, it is energetically favorable to be magnetized in specific directions, commonly referred to as anisotropy axes. The origin of magnetic anisotropy is in the symmetry properties of the electrostatic field in the material, which originate from the symmetry properties of the atomic lattice. The interaction of this background field in the lattice and the individual magnetic moments causes certain directions to have lower energies for the magnetic moments. [4]

Multiple types of anisotropy exist, the characterizing aspects being the number of anisotropy axes and the displayed crystal symmetry. In this work, only uniaxial anisotropy will be considered. Uniaxial anisotropy is characterized by the presence of only one anisotropy axis. It needs to be noted that when considering energy minimization, the direction of the magnetization along the anisotropy axis does not matter. Both directions along the axis are energetically equally favored, making the domain structure presented in Chapter 3 more realistic from this perspective. [21]

If a uniaxial anisotropy is assumed along an arbitrary x-direction, the resulting $\boldsymbol{H}_{\mathrm{an}}$ has only the x-component. The field strength can be expressed in terms of M as [2]

$$H_{\mathrm{an,x}} = \frac{2K_{\mathrm{u}}}{\mu_0 M_{\mathrm{s}}^2} M_{\mathrm{x}}. \tag{4.4}$$

The parameter K_{u} in (4.4) is the anisotropy constant which describes the strength of anisotropic effects. Despite its name, K_{u} is not strictly speaking a material or geometry dependent constant because it depends on the annealing treatment prior done to the sample [8, 12].

Magnetostatic field

The origin of the magnetostatic field $\boldsymbol{H}_{\mathrm{ms}}$ is the elementary magnetic dipole moments in the material. Each magnetic moment causes a field, and $\boldsymbol{H}_{\mathrm{ms}}$ is the sum of these fields. The magnetostatic field is a long-range interaction. The position and orientation of each magnetic moment affect $\boldsymbol{H}_{\mathrm{ms}}$ in every point in the material. Thus, $\boldsymbol{H}_{\mathrm{ms}}$ does not only
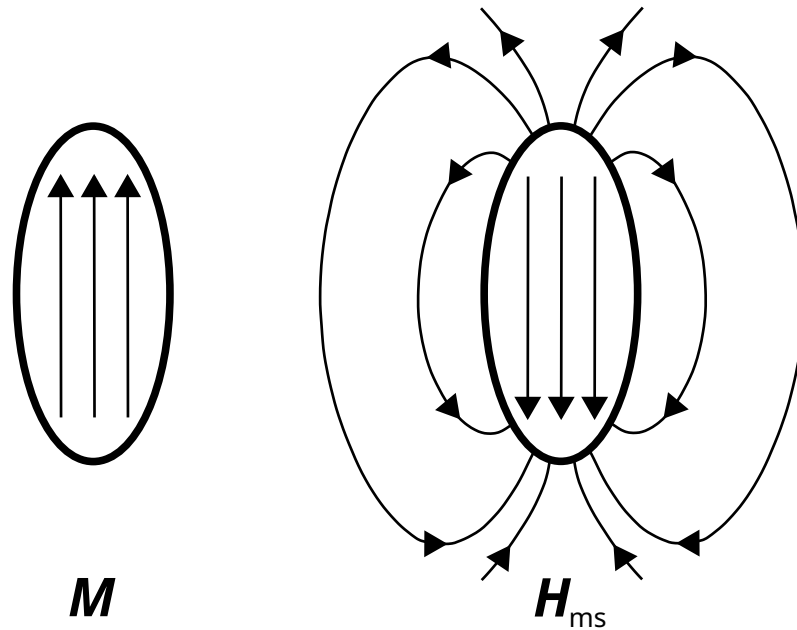
Figure 4.2. *Magnetostatic field caused by a uniformly magnetized ellipsoidal body. Exceptionally, H_{ms} is also uniform inside the body under these conditions.*

depend on M but also the geometrical shape of the system. The field in an arbitrary point w_0 can be expressed in a general form as

$$H_{\mathrm{ms}}(w_0) = \frac{1}{4\pi} \int_V \nabla \frac{\nabla \cdot M(r')}{\|w_0 - r'\|} dr' - \frac{1}{4\pi} \int_S \nabla \frac{\hat{e}_{\mathrm{n}} \cdot M(r')}{\|w_0 - r'\|} da',$$ (4.5)

where $\int_V dr'$ is an integral over the volume, $\int_S da'$ an integral over the surface of the geometry, and $\hat{e}_{\mathrm{n}}$ the normal vector of the surface. [4]

The structure of (4.5) is rather complex. In general situations, the evaluation of H_{ms} requires by far the most computational resources from the contributions of H_{eff} [21]. In large simulations, calculation of H_{ms} can be a significant factor in the total computing time. However, there exist particular situations in which (4.5) takes a simpler form. Under a uniform M in a system of ellipsoidal shape (e.g. a sphere), H_{ms} is also uniform and can be evaluated as a product of M and geometry dependent constants. In the described situation, H_{ms} inside the material points to the opposite direction of M. The magnetostatic field is often referred to as the *demagnetizing field* because H_{ms} tends to oppose M. Figure 4.2 illustrates H_{ms} created by a uniformly magnetized ellipsoid. Generally, H_{ms} cannot be assumed to be uniform even if M would be. Methods exist to calculate averaged geometry dependent constants in order to calculate H_{ms} as in ellipsoidal geometries. For example for rectangular prisms (e.g. a cube) with uniform M, analytical expressions exist [24].

When examining a tape wound core, direct evaluation of (4.5) is not feasible. Additionally, the type of simplifications discussed above are not inherently present in the situation

despite the assumed simple domain structure of the tape. In this work, some additional assumptions are introduced to approximate $\boldsymbol{H}_{\mathrm{ms}}$. The goal is to separate $\boldsymbol{M}$ and a geometry dependent matrix $\boldsymbol{N}$. The separation ensures that $\boldsymbol{N}$ becomes constant, and $\boldsymbol{H}_{\mathrm{ms}}$ can be evaluated with a low computational burden. The used approximation utilizes a similar approach to what is used in [2].

Despite modeling tape wound cores, the calculation of $\boldsymbol{H}_{\mathrm{ms}}$ is carried out for a single strip of tape. Effectively, the curvature and neighboring tape layers are neglected. DWs are not taken into account, and the tape is assumed to consist of opposite-facing domains with negligible boundaries. With these assumptions, the calculation of $\boldsymbol{H}_{\mathrm{ms}}$ along the tape thickness reduces to a sum of individual domain contributions along the v-axis when the coordinate system of Figure 3.3 is used. When additionally $\boldsymbol{M}$ is treated as if it were uniform despite $\boldsymbol{M} = \boldsymbol{M}(w)$, the integral over volume in (4.5) can be neglected because $\nabla \cdot \boldsymbol{M} = 0$. The magnetostatic field is written as

$$\boldsymbol{H}_{\mathrm{ms}}(\boldsymbol{w}_0) = \frac{1}{4\pi} \sum_{n=-N}^{N} \int_{S_n} (\hat{\boldsymbol{e}}_{\mathrm{n}} \cdot \boldsymbol{M}) \frac{\boldsymbol{w}_0 - \boldsymbol{r}'}{\|\boldsymbol{w}_0 - \boldsymbol{r}'\|^3} da', \tag{4.6}$$

where also the result $\nabla \frac{1}{\|\boldsymbol{r}-\boldsymbol{r}'\|} = -\frac{\boldsymbol{r}-\boldsymbol{r}'}{\|\boldsymbol{r}-\boldsymbol{r}'\|^3}$ is used. When (4.6) is evaluated, the contribution of $2N + 1$ domains is taken into account. The description includes N neighboring domains in both directions along the v-axis, and the domain for which $\boldsymbol{H}_{\mathrm{ms}}$ is being evaluated. When $\boldsymbol{H}_{\mathrm{ms}}$ is calculated over the thickness of the tape, (4.6) eventually reduces to

$$\boldsymbol{H}_{\mathrm{ms}}(w) = \boldsymbol{N}\boldsymbol{M}(w). \tag{4.7}$$

Appendix A shows the calculation how matrix $\boldsymbol{N}$ is obtained. According to the approximations done earlier, (4.7) is evaluated with a non-uniform $\boldsymbol{M}(w)$ despite $\boldsymbol{N}$ is determined by assuming a uniform $\boldsymbol{M}$.

In literature, also simpler methods to approximate $\boldsymbol{H}_{\mathrm{ms}}$ caused by the domain structure of the tape are used [3, 25]. In these approximations, the magnetostatic field is assumed to have only the component in the direction of the tape thickness, and it is calculated as a product of the parallel component of $\boldsymbol{M}$ and a constant: $H_{\mathrm{ms,w}} = -\mathrm{constant} \cdot M_{\mathrm{w}}$. These approaches assume that the DWs and demagnetizing effects at tape edges can be neglected [25].

The discussed examples of $\boldsymbol{H}_{\mathrm{ms}}$ calculation utilize the simplicity of $\boldsymbol{M}$ to at least approximately simplify (4.5). In situations with more complex spatial dependency on $\boldsymbol{M}$, a different approach is required. A method to calculate $\boldsymbol{H}_{\mathrm{ms}}$ in finite difference micromagnetics by utilizing fast Fourier transforms is briefly mentioned because of its benefits and

extensive use. The main idea is to accelerate the calculation by evaluating the convolution structure of (4.5) in the Fourier space. This reduces the computational burden from $\mathcal{O}(N_{\mathrm{cell}}^2)$ to $\mathcal{O}(N_{\mathrm{cell}} \log N_{\mathrm{cell}})$, where N_{cell} is the number of finite difference cells. More details on the fast Fourier transform based method can be found, for example, in [21] or [26]. However, $\boldsymbol{M}$ in the tape exhibits a high amount of spatial symmetry. Consequently, the approximate analytical method to evaluate $\boldsymbol{H}_{\mathrm{ms}}$ (4.7) is used in this work.

External field

The separation of the external field $\boldsymbol{H}_{\mathrm{a}}$ and eddy current field $\boldsymbol{H}_{\mathrm{eddy}}$ is a quite vague concept, as the field caused by $\boldsymbol{H}_{\mathrm{a}}$ inside a conducting medium is a sum of these fields. Still, this division is used to express both the field in and outside of the tape material. The external field $\boldsymbol{H}_{\mathrm{a}}$ is sometimes, also in this work, presented as the external magnetic flux density. These quantities are connected through (2.1) and by using $\mu = \mu_0$. This aspect will be covered in the coming sections when the derivation of the developed model is shown.

According to classical physics, a magnetic moment in an external field tends to align itself with the field. When the other micromagnetic field contributions are taken into account, this is not necessarily the case. However, introducing an external field pointing in another direction gives the system potential energy, which affects the micromagnetic total energy. The energy contribution originating from the external field is often referred to as the *Zeeman energy* [20].

Eddy current field

The eddy current field $\boldsymbol{H}_{\mathrm{eddy}}$ is created to the conducting medium because of macroscopic eddy currents induced by an external field. Generally, $\boldsymbol{H}_{\mathrm{eddy}}$ decreases the effect of $\boldsymbol{H}_{\mathrm{a}}$ inside the material, the effect being stronger deeper in the material. This causes the resulting field to have a spatial dependency along the material thickness. This effect is amplified when the frequency of the external field is increased. [4]

Eddy current effects are often modeled with a diffusion equation, for example (3.5) for the 1D case [6]. In this work, however, the eddy current problem is solved with (3.7) following the discussion of Chapter 3. H_{eddy} is approximated as a scalar field because of the tape material, which is thin from the perspective of eddy current modeling. In this work, quite unconventionally in the domain of micromagnetics, the used criteria for the discretization length along the tape thickness is the accurate modeling of H_{eddy}.

4.1.3 Time discretization of the LLG-equation

Equation (4.1) needs to be modified slightly in order to solve it numerically. The time derivative of M needs to be discretized, but the requirement of constant $\|M\|$ makes the process more complicated. Also, attention has to be paid to how the system's initial state is determined and how the calculation workflow proceeds.

The constraint of constant $\|M\|$ with discrete time-stepping can be satisfied by using a norm-conserving formalism for the magnetization updating. The adopted method is based on the Cayley transform and skew-symmetric matrices, and the underlying time discretization itself is done with the Euler method. A sufficiently small timestep $\Delta t \sim 1\,\mathrm{ps}$ should be used to model the LLG dynamics correctly. [2, 27]

In order to solve the time evolution of M, the initial magnetization field alongside many simulation-specific parameters have to be known. The assumed domain structure of the tape material gives a good first estimation for the initial M which can further be improved by using a suitable 1D time-harmonic model presented in [3]. Despite this, a startup transient is expected when the time-stepping is begun. This is because of the differences between the time-harmonic and time-stepping models and the lack of micromagnetic energy minimization procedure after evaluating the 1D time-harmonic model. Often in micromagnetic software, for example, in MuMax3 [28], there is an energy minimization procedure implemented to approximate the steady-state in situations where the external field is not imposed.

When the magnetization field from the previous timestep $k-1$ is known, many terms of the effective magnetic field can be evaluated. The following iteration proceeds through the entire computation: H_{eff}^{k-1} is determined by using M^{k-1} and then M^k is solved from the LLG equation by using H_{eff}^{k-1}. In a way, it can be said that M^k is determined by using the H_{eff} from the previous timestep. The only exceptions for this convention are H_{eddy} and H_{a} which are solved for the same step for which the magnetization is being updated to.

4.1.4 Simulation properties

3D micromagnetic simulations can be carried out relatively easily by using dedicated software. In this work, the simulations are performed with MuMax3: a GPU accelerated micromagnetic simulation program [28]. These simulations aim to provide one additional method to determine the losses and to observe the spatial variations of M in the tape. In principle, also the dependency of the DW processes on the excitation frequency can be studied.

The primary difficulty in carrying out 3D micromagnetic simulations is managing the com-

putational burden. For example, when the width of the domain is assumed to be in the range of $100\,\mu\text{m}$, the tape thickness approximately $10\,\mu\text{m}$ and the tape width is much greater than the domain width, already the simulation of a single domain is impossible due to computational burden. MuMax3 is set to discretize the 3D space with a discretization length in the range of nanometers leading to a large number of degrees of freedom to be solved. A point worth mentioning is that MuMax3 discretizes the space with a finite difference mesh, i.e., all the unit volumes are identical rectangular cuboids. The computational burden is also significantly increased because of the need to use small Δt in micromagnetic simulations. Altogether, it can be said that the spatial scale of the tape is out of the scope of micromagnetic simulations, and some approximations are required when attempting to study an entire tape wound core.

The chosen approach is to divide the domain structure of the tape material into parts corresponding to the assumed loss mechanisms. A uniformly magnetized region from the center of a domain and a region containing a DW are simulated independently. When simulating a DW, the simulation size has to be set large enough to encapsulate the DW activity caused by the applied field. The main assumption behind this approach is that these separately simulated systems can be examined independently, meaning that the interaction between domains and DWs can be neglected to some extent. In other words, the assumption is that the DWs do not affect the uniform magnetization in the middle of the domain and vice versa.

In both of these simulations, periodic boundary conditions (PBC) can be used to reduce computational burden further. In MuMax3, PBCs are implemented so that the user can determine how many periodic repetitions of the system are wanted in each direction. The advantage of using PBCs is that in the directions in which the simulated body is symmetric, the size of the simulated region can be reduced.

The power losses in the simulation region can be determined by using the simulation outputs of MuMax3. MuMax3 is capable of outputting the necessary field quantities over the simulated time. The power losses can be determined by using the equation [29]

$$p = \frac{1}{V} \frac{\alpha_{\text{G}} \mu_0^2 \left| \gamma_G \right| V_{\text{cell}}}{(1 + \alpha_{\text{G}}^2) M_{\text{s}}} \sum_{i=1}^{N_{\text{cell}}} (\boldsymbol{M}_i \times \boldsymbol{H}_{\text{eff},i})^2 \tag{4.8}$$

which can be modified to the form

$$p = \frac{\alpha_{\text{G}} \left| \gamma_G \right| M_{\text{s}}}{(1 + \alpha_{\text{G}}^2) N_{\text{cell}}} \sum_{i=1}^{N_{\text{cell}}} (\boldsymbol{m}_i \times \boldsymbol{B}_{\text{eff},i})^2 \tag{4.9}$$

in order to express the losses in terms of $\boldsymbol{m}$ and $\boldsymbol{B}_{\text{eff}}$, quantities available as simulation outputs. The relative magnetization $\boldsymbol{m}$ is obtained when $\boldsymbol{M}$ is normalized with respect

to M_{s}: $\boldsymbol{m} = \frac{\boldsymbol{M}}{M_{\mathrm{s}}}$. The effective magnetic flux density $\boldsymbol{B}_{\mathrm{eff}}$ is connected to $\boldsymbol{H}_{\mathrm{eff}}$ through $\boldsymbol{B}_{\mathrm{eff}} = \mu_0 \left(\boldsymbol{H}_{\mathrm{eff}} + \boldsymbol{M} \right)$. In (4.8 - 4.9), V_{cell} is the volume of a discretization cell. Equation (4.9) gives the instantaneous power loss density which needs to be integrated over an excitation period in order to obtain the loss per cycle.

4.2 1D micromagnetic model with eddy currents

The approximate solution of the 1D diffusion equation that was presented in Chapter 3 can be combined with the micromagnetic theory to obtain a model utilizing a micromagnetic material property. This model can solve the eddy current problem over the thickness of the tape with the micromagnetic material property. Therefore, it will be referred to as the 1D micromagnetic model with eddy currents.

As the LLG-equation is to be used as the material property, it is convenient to take it as the starting point of the model derivation. When the time derivative of $\boldsymbol{M}$ is discretized with the Euler method and some rearranging of terms is done, the equation can be written as

$$\boldsymbol{M}^k = \boldsymbol{M}^{k-1} - \frac{\Delta t \left| \gamma_{\mathrm{G}} \right| \mu_0}{1 + \alpha_{\mathrm{G}}^2} \boldsymbol{M}^{k-1} \times \left(\left(\boldsymbol{I} + \frac{\alpha_{\mathrm{G}}}{M_{\mathrm{s}}} \boldsymbol{M}^{k-1} \times \right) \boldsymbol{H}_{\mathrm{eff}}^{k-1} \right), \qquad (4.10)$$

where $\boldsymbol{I}$ is an identity matrix. Importantly, now the Cayley transform based approach was not used to discretize the LLG equation. This helps to simplify the model and the norm conservation is ensured at latter phases of calculation. The effective field can be expressed as a sum of two subsums, denoted as $\boldsymbol{H}_{\mathrm{ex,an,ms}} = \boldsymbol{H}_{\mathrm{ex}} + \boldsymbol{H}_{\mathrm{an}} + \boldsymbol{H}_{\mathrm{ms}}$ and $H_{\mathrm{a,eddy}} \hat{\boldsymbol{e}}_{\mathrm{v}} = (H_{\mathrm{a}} + H_{\mathrm{eddy}}) \hat{\boldsymbol{e}}_{\mathrm{v}}$, where $\hat{\boldsymbol{e}}_{\mathrm{v}}$ is a unit vector in the v-direction in the coordinate system of Figure 3.3. Using this notation, the v-component of the magnetization can be expressed as

$$\begin{aligned} M_{\mathrm{v}}^k = M_{\mathrm{v}}^{k-1} - \frac{\Delta t \left| \gamma_{\mathrm{G}} \right| \mu_0}{1 + \alpha_{\mathrm{G}}^2} &\left[\boldsymbol{M}^{k-1} \times \left(\left(\boldsymbol{I} + \frac{\alpha_{\mathrm{G}}}{M_{\mathrm{s}}} \boldsymbol{M}^{k-1} \times \right) \boldsymbol{H}_{\mathrm{ex,an,ms}}^{k-1} \right) \right] \cdot \hat{\boldsymbol{e}}_{\mathrm{v}} \\ &+ \frac{\Delta t \left| \gamma_{\mathrm{G}} \right| \mu_0}{1 + \alpha_{\mathrm{G}}^2} \frac{\alpha_{\mathrm{G}}}{M_{\mathrm{s}}} \left((M_{\mathrm{u}}^{k-1})^2 + (M_{\mathrm{w}}^{k-1})^2 \right) H_{\mathrm{a,eddy}}^k \end{aligned} \quad (4.11)$$

which can be abbreviated to

$$M_{\mathrm{v}}^k(w) = a(w) + c(w) H_{\mathrm{a,eddy}}^k(w) \qquad (4.12)$$

in order the emphasize the dependency of M_{v}^k from $H_{\mathrm{a,eddy}}^k$. The dependencies from w are added to (4.12) to remind that the quantities vary spatially only along the thickness of

the tape. The field $H_{\text{a,eddy}}^k$ is the magnetic field strength induced to a body by the effect of an external field. It can be expressed as

$$H_{\text{a,eddy}}(w) = \nu_0 \boldsymbol{\alpha}^{\text{T}}(w)\boldsymbol{b} - M_{\text{v}}(w) \tag{4.13}$$

by utilizing (2.2) and (3.6). The reluctivity of free space ν_0 is introduced to slightly simplify the notation. Finally combining (4.12) and (4.13), and solving for M_{v}^k we get

$$M_{\text{v}}^k(w) = \frac{a(w)}{1 + c(w)} + \frac{c(w)}{1 + c(w)}\nu_0 \boldsymbol{\alpha}^{\text{T}}(w)\boldsymbol{b}^k \tag{4.14}$$

which is the desired result from the considerations starting from the LLG equation.

To obtain the 1DMMEC model, the result above needs still to be combined with (3.7). Utilizing once more (2.2) and writing the equation for time instance k, the vector $\boldsymbol{h}_{\text{s}}$ is equal to

$$\boldsymbol{h}_{\text{s}}^k = \frac{1}{d}\int_{-d/2}^{d/2} \boldsymbol{\alpha}(w)\left(\nu_0 \boldsymbol{\alpha}^{\text{T}}(w)\boldsymbol{b}^k - M_{\text{v}}^k(w)\right) dw + \sigma d^2 \boldsymbol{C}\left(\frac{\partial \boldsymbol{b}}{\partial t}\right)^k. \tag{4.15}$$

Combining (4.14) and (4.15) and rearranging the terms, the result can be expressed as

$$\begin{aligned} \boldsymbol{h}_{\text{s}}^k = \boldsymbol{V}\boldsymbol{b}^k + \sigma d^2 \boldsymbol{C}\left(\frac{\partial \boldsymbol{b}}{\partial t}\right)^k - \frac{1}{d}\int_{-d/2}^{d/2}\frac{a(w)}{1+c(w)}\boldsymbol{\alpha}(w)dw \\ - \frac{1}{d}\int_{-d/2}^{d/2}\frac{c(w)}{1+c(w)}\nu_0\boldsymbol{\alpha}(w)\boldsymbol{\alpha}^{\text{T}}(w)\boldsymbol{b}^k dw, \end{aligned} \tag{4.16}$$

where matrix $\boldsymbol{V}$ is defined as

$$\boldsymbol{V} = \frac{\nu_0}{d}\int_{-d/2}^{d/2}\boldsymbol{\alpha}(w)\boldsymbol{\alpha}^{\text{T}}(w)dw. \tag{4.17}$$

The time derivatives of the magnetic flux density coefficients are evaluated with Euler discretization. Equation (4.16) is the 1DMMEC model, and by solving it, an approximate solution to the eddy current problem with micromagnetic material property is obtained. The average magnetic flux density b_0 is given to the model as an input, and by solving the time evolution of h_{s}, the power losses can be calculated with (3.4).

It needs to be noted that in order to integrate (4.16) over time, also the LLG equation needs to be solved for every timestep to obtain the time evolution of $\boldsymbol{M}$. In comparison to (4.10) this time the time-stepping is done with the Cayley-formalism mentioned earlier in

this chapter to ensure the conservation of $\|\boldsymbol{M}\|$. After the solution of (4.16) is obtained, $H^k_{\mathrm{a,eddy}}$ can be calculated and fed forward in order to solve the LLG equation for $\boldsymbol{M}^k$.

4.3   2D finite element method

This section briefly introduces FEM. As the topic is vast, we will limit ourselves to a quick overview and go only into details in the concepts essential in the model developed in this work. Plenty of literature exists on the topic. For example, [30] gives a detailed introduction to FEM, and [31] emphasizes on FEM applied to electromagnetism.

FEM can approximate solutions to partial differential equation (PDE) systems. The solution domain Ω is discretized into a finite number of elements, and the approximate solution is expressed in terms of chosen shape functions W_i. This work uses the Galerkin weighted residual method to carry out the finite element analysis (FEA). Also, we restrict to 2D FEM, and the modeling domain consists of an axial cross-section of the tape wound core, the winding conductors, and the surrounding air. Carrying out 2D FEA greatly reduces the computational burden compared to full 3D analysis.

FEA is utilized in this work to obtain the magnetic fields over the cross-section of the tape wound core. The PDE to be solved is obtained from the *quasi-static* Maxwell's equations. It is beneficial to formulate the problem in terms of the magnetic vector potential $\boldsymbol{A}$ which is defined as

$$\boldsymbol{B} = \nabla \times \boldsymbol{A}. \tag{4.18}$$

Obtaining the solution by using $\boldsymbol{A}$ is particularly attractive in 2D analysis because in such cases, $\boldsymbol{A}$ reduces to a scalar field.

The solution that is obtained from the system of equations formed with FEM is the nodal values of magnetic vector potential $\boldsymbol{a}$. A value is obtained for each defined nodal point in Ω. The continuous magnetic vector potential field can be expressed in the coordinate system of Figure 3.2 by using the shape functions as

$$A(x,y) = \sum_{i=1}^{N_{\mathrm{p}}} W_i(x,y)a_i, \tag{4.19}$$

where N_{p} is the number of nodal points. The shape functions interpolate the value of $\boldsymbol{A}$ between separate nodal points.

Some simplifying modifications are done to the tape wound core geometry of Figure 3.2 to allow for more computationally efficient FEA. The spiral shape of the geometry is ignored, and instead, it is thought to consist of circular layers of tape. This approximation is

reasonable when the tape is thin. Additionally, every tape layer is not modeled separately, but instead, *homogenization* of the core region is utilized. From the perspective of 2D FEA, the core region is seen as a solid object. The region is divided into elements larger than the tape thickness, and the effect of the layered structure is taken into account with the 1DMMEC model presented in the previous section. The 1DMMEC model is evaluated in every nodal point of Ω. The effect of tape layers can be taken into account less frequently compared to how many layers exist in the core because h_s and b_0 are expected to vary little from one tape layer to the next [32]. Given this, the losses calculated from (3.4) for the homogenized core are expected to approximate well the losses in the actual geometry. Homogenization of the core neglects the effects of the insulation between separate tape layers. Direct modeling of the core with all its tape layers would lead to a poor computational performance [32].

Because the conductors around the tape wound core are also included in Ω, the conductor voltages u and currents i have to be solved. The equations governing u and i are derived from circuit theory. These equations are coupled with the field equations by using an AVI-formulation and from the solution of the coupled system of equations a, u and i are obtained. More details on the coupling of field and circuit equations are given, for example, in [33].

4.4   Coupled 1D micromagnetic – 2D FE model

The 2D FEM and 1DMMEC model from the previous sections can be combined to form the 1DMMEC–2DFE model. The resulting model approximates the tape wound core in 2D over its cross-section and assumes a micromagnetic material property for the tape material. In comparison to the 1DMMEC model, this model takes into account the spatial variation of the fields over the core cross-section. In this section, the 1DMMEC–2DFE model is presented. Additionally, the method used to solve the resulting system of equations is discussed.

When shifting the focus from the previous 1D considerations to a 2D modeling domain, some changes to the modeling approach have to be made. A circulating flux in the cross-section of the tape wound core cannot be taken into account with a single coordinate in Cartesian coordinates. However, using radial and tangential coordinates proves to be beneficial. In the coordinate system of Figure 3.2 the 2D magnetic field strength H can be expressed as

$$\boldsymbol{H} = \begin{bmatrix} H_{\mathrm{rad}} \\ H_{\mathrm{tan}} \end{bmatrix}. \tag{4.20}$$

The transformation from Cartesian coordinates to tangential and radial components can

be performed with a rotation matrix $\boldsymbol{R}$. By multiplying $\boldsymbol{R}$ with $\boldsymbol{H}$ in radial and tangential components, the magnetic field in Cartesian coordinates is obtained

$$\begin{bmatrix} H_{\mathrm{x}} \\ H_{\mathrm{y}} \end{bmatrix} = \underbrace{\begin{bmatrix} \cos(\phi) & -\sin(\phi) \\ \sin(\phi) & \cos(\phi) \end{bmatrix}}_{\boldsymbol{R}} \begin{bmatrix} H_{\mathrm{rad}} \\ H_{\mathrm{tan}} \end{bmatrix}. \tag{4.21}$$

The coordinate transformation in the other direction is obtained simply by multiplying the inverse of the rotational matrix $\boldsymbol{R}^{-1}$ with $\boldsymbol{H}$ in Cartesian coordinates. The inverse $\boldsymbol{R}^{-1}$ is equal to $\boldsymbol{R}^{\mathrm{T}}$.

Due to the circular geometry of the core, magnitudes of tangential components of the fields are expected to dominate. Also, the tangential magnetic flux density can be considered as the input for (4.16) when the slight radial shift between separate tape layers is neglected. The radial field quantities are assumed to be small, and thus, the permeability of free space is used as the material property in the radial direction.

When (4.16) is used to evaluate the tangential component of the magnetic field strength at the surface of the tape, N_{b} magnetic flux density coefficients enter the 2D calculation. Coefficients b_n are solved at every integration point of the 2D geometry. This can be interpreted as if the spatial distribution of each coefficient b_n would create a magnetic flux density field over the tape wound core cross-section. Each of these fields can be expressed with a corresponding magnetic vector potential $\boldsymbol{a}_n$. The existence of the contributions in the radial direction makes the situation more complicated. Even a small radial contribution would violate the assumption of scalar field quantities used in the derivation of (4.16). Additionally, the physical meaning of coefficients b_n in the radial direction is unclear. A perfectly circulating magnetic flux density in the tape wound core cross-section would remove the radial effects entirely. As the solution is obtained with numerical methods, it is concluded that a small magnetic flux density approximated with a cosine series also exists in the radial direction due to numerical error.

With the help of the considerations above, the equations for FEA in the core region can be derived. The domain Ω refers explicitly to the core region in the following. When forming the total system matrices, the air and conductor regions are handled with commonly used FEA practices. The magnetic field strength $\boldsymbol{H}_{\mathrm{s},m}$ is defined to be a 2D vector field containing the values of the mth radial and tangential components of the respective 2D field. The matrix $\boldsymbol{H}_{\mathrm{s}}$ containing the values of all the N_{b} 2D field terms is assumed to be structured in a similar way as $\boldsymbol{h}_{\mathrm{s}}$ in (4.16): apart from the first row, all the entries are 0. Thus, $\boldsymbol{H}_{\mathrm{s},0}$ gives the 2D magnetic field strength at the surface of the tape. Equation $\nabla \times (\boldsymbol{R}\boldsymbol{H}_{\mathrm{s},m}) = \boldsymbol{0}$ in Cartesian coordinates is taken as the starting point, and its weak

form can be written as

$$\boldsymbol{r}_{\mathrm{a}m} = \int_{\Omega} \boldsymbol{W} \cdot [\nabla \times (\boldsymbol{R}\boldsymbol{H}_{\mathrm{s},m})]\, d\Omega = \boldsymbol{0}, \tag{4.22}$$

which can further be expressed as

$$\boldsymbol{r}_{\mathrm{a}m} = \int_{\Omega} (\nabla \times \boldsymbol{W}) \cdot \boldsymbol{R}\boldsymbol{H}_{\mathrm{s},m}\, d\Omega \tag{4.23}$$

by using Green's theorem and assuming that inhomogeneous Neumann conditions are not present [31]. The weak form is written in terms of vector $\boldsymbol{W}$ containing the shape functions W_i. This can be done because the Galerkin method is used. Notation $\boldsymbol{r}_{\mathrm{a}m}$ is used to denote that the presented equations express a part of the total residual $\boldsymbol{r}$ that originate from the mth magnetic vector potential field. Equation (4.23) can be written as

$$\boldsymbol{r}_{\mathrm{a}m} = \int_{\Omega} \boldsymbol{D}^{\mathrm{T}}\boldsymbol{R}\boldsymbol{H}_{\mathrm{s},m}\, d\Omega, \tag{4.24}$$

when the 2D discrete curl operator $\boldsymbol{D}$ is introduced [18]

$$\boldsymbol{D} = \begin{bmatrix} \dfrac{\partial W_1}{\partial y} & \dfrac{\partial W_2}{\partial y} & \cdots & \dfrac{\partial W_{N_{\mathrm{p}}}}{\partial y} \\[2ex] -\dfrac{\partial W_1}{\partial x} & -\dfrac{\partial W_2}{\partial x} & \cdots & -\dfrac{\partial W_{N_{\mathrm{p}}}}{\partial x} \end{bmatrix}. \tag{4.25}$$

Now $H_{\mathrm{s},m,\tan}$ can be calculated from (4.16) and $H_{\mathrm{s},m,\mathrm{rad}}$ from the corresponding radial component of the magnetic flux density. When some rearranging of terms is done and short-hand notation used, the result can be written as

$$\boldsymbol{r}_{\mathrm{a}m} = \int_{\Omega} \boldsymbol{D}^{\mathrm{T}}\boldsymbol{R} \left(\sum_{n=0}^{N_{\mathrm{b}}-1} \left(\begin{bmatrix} \nu_0 \delta_{mn} & 0 \\ 0 & V_{mn} + \frac{\sigma d^2}{\Delta t} C_{mn} - G_{mn} \end{bmatrix} \begin{bmatrix} B^k_{n,\mathrm{rad}} \\ B^k_{n,\tan} \end{bmatrix} \right) - \begin{bmatrix} 0 \\ F_m \end{bmatrix} \right) d\Omega \tag{4.26}$$

where $B^k_{n,\mathrm{rad}}$ and $B^k_{n,\tan}$ are the radial and tangential components of the nth magnetic flux density field at timestep k. Vector $\boldsymbol{F}$ contains the terms independent of $B^k_{n,\mathrm{rad}}$ and $B^k_{n,\tan}$, and δ_{mn} is the *Kronecker delta*. The matrix $\boldsymbol{G}$ is short-hand notation for

$$\boldsymbol{G} = \frac{\nu_0}{d} \int_{-d/2}^{d/2} \frac{c(w)}{1+c(w)} \boldsymbol{\alpha}(w)\boldsymbol{\alpha}^{\mathrm{T}}(w)\, dw. \tag{4.27}$$

The subscript m in matrices $\boldsymbol{V}$, $\boldsymbol{C}$ and $\boldsymbol{G}$, and vector $\boldsymbol{F}$ expresses explicitly that the mth

row is substituted to (4.26). Indexing with n selects the nth entry of a vector regardless if the vector is a row or a column vector.

Quite remarkably, the derived residual vector is linear with respect to B, or alternatively to a because $B_m = Da_m$, and could be solved directly. However, the system of equations is solved with Newton-Raphson iteration to allow utilizing some previously made code that is available. When solving a linear system with numerical iteration, the computational burden of the solution increases. After the first round of iteration, a second iteration has to be executed until convergence is observed.

The Newton-Raphson iteration is carried out as

$$x_{i+1} = x_i - J(x_i)^{-1} r(x_i) \tag{4.28}$$

where x is a vector of the quantities to be solved, in this case $x = \begin{bmatrix} a & u & i \end{bmatrix}^{\text{T}}$. In order to carry out the iteration, the Jacobian matrix J contributions from the core region need to be determined. When (4.26) for the mth vector potential field is differentiated in respect to a_n the corresponding contribution to the total Jacobian reads

$$J_{aman} = \int_{\Omega} D^{\text{T}} R \begin{bmatrix} \nu_0 \delta_{mn} & 0 \\ 0 & V_{mn} + \frac{\sigma d^2}{\Delta t} C_{mn} - G_{mn} \end{bmatrix} R^{\text{T}} D d\Omega. \tag{4.29}$$

For completeness, below are expressed the total residual vector and Jacobian matrix from which the system of equations can be solved by using (4.28). The total residual reads

$$r = \begin{bmatrix} r_{a0} & r_{a1} & \ldots & r_{am} & r_{u} & r_{i} \end{bmatrix}^{\text{T}}, \tag{4.30}$$

in which r_{u} and r_{i} are the residuals corresponding to the circuit equations. The Jacobian matrix can be expressed as

$$J = \frac{\partial r}{\partial x} = \begin{bmatrix} J_{a0a0} & J_{a0a1} & \ldots & J_{a0am} & J_{a0u} & J_{a0i} \\ J_{a1a0} & J_{a1a1} & \ldots & J_{a1am} & 0 & 0 \\ \vdots & & & \vdots & \vdots & \vdots \\ J_{ama0} & J_{ama1} & \ldots & J_{amam} & 0 & 0 \\ J_{ua0} & 0 & \ldots & 0 & J_{uu} & J_{ui} \\ J_{ia0} & 0 & \ldots & 0 & J_{iu} & J_{ii} \end{bmatrix}. \tag{4.31}$$

The submatrices J_{au}, J_{ai}, J_{ua} and J_{ia} result from the coupling of the field problem to the circuit equations which depend only on a_0. The higher-order a terms do not contribute to

the circuit equations. Differentiation with respect to higher-order magnetic vector potential fields evaluates to 0, and effectively J is zero-padded to a square matrix from these parts. The degrees of freedom corresponding to boundary nodes of the finite element mesh have to be modified to include the desired boundary conditions.

5 RESULTS AND DISCUSSION

This chapter presents the results that are obtained with the methods of Chapter 4. The emphasis is on the predicted iron losses, but also other topics are discussed according to the properties of each approach. Comparisons are made between the different approaches and results presented in the literature to evaluate the performance of the used methods.

5.1 3D micromagnetic simulations

The domain and DW in the domain structure of the tape material (see Figure 3.3) are simulated separately with MuMax3. First, the simulation of the domain region is examined. Figure 5.1 presents the simulated power dissipation, losses determined with a 1D time-harmonic model [3], and the measured losses for a $Co_{71}Fe_4B_{15}Si_{10}$ tape wound core with tape thickness of $17\,\mu m$ [2]. The simulated losses were calculated with (4.9) using the material parameters of $Co_{71}Fe_4B_{15}Si_{10}$ [2]. The same material parameters were used with the 1D time-harmonic model. The used 1D time-harmonic model is quite similar to the 1DMMEC model that was presented in Chapter 4. Both models solve the eddy current problem in 1D over the thickness of the tape and take into account a micromagnetic material property. The 1D time-harmonic model is an analytical approach with some additional simplifying assumptions and does not require time-stepping to solve the system.

The simulated part of a domain was set to be over the entire tape thickness, whereas on the surfaces, a very small part of the actual domain surface was considered. On the domain surface, a large number of periodic repetitions were used in both directions on the plane. It was observed that the dissipated power depends on the number of periodic repetitions used. The used value in this work is a compromise between computational performance and keeping the geometric shape of the system similar to the actual domains of the tape.

Figure 5.1 shows that the simulated losses are lower than the losses predicted by the 1D time-harmonic model and the measured losses. However, all the presented losses increase as a function of frequency, and the difference between the simulated result and the other plots decreases with increasing frequency. The consistently lower losses are expected because the eddy current related phenomena are neglected due to code re-
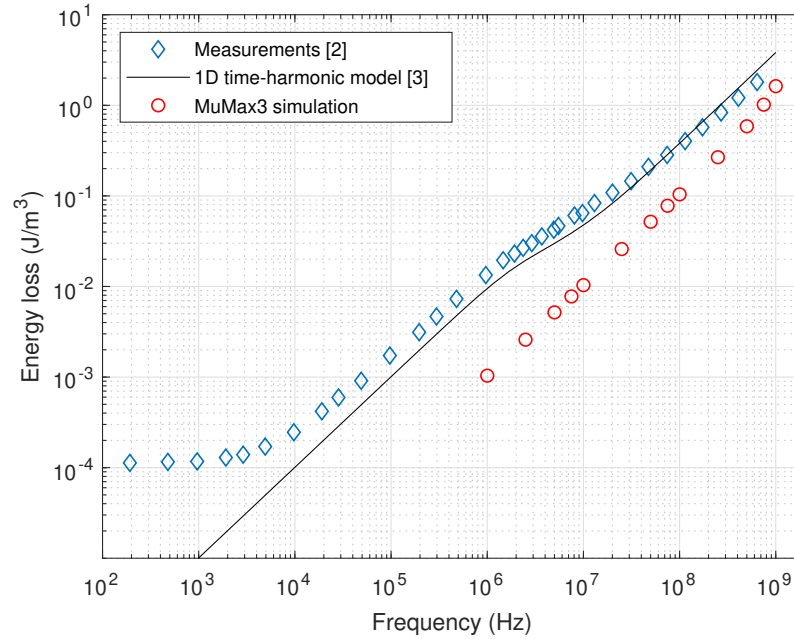
Figure 5.1. *Comparison of simulated losses, measurements, and 1D time-harmonic model results for 17 μm thick $Co_{71}Fe_4B_{15}Si_{10}$. The simulated losses consider only the domain region and neglect eddy currents. Consistently lower simulated losses are assumed to be caused by the missing eddy current contribution and neglected structural disorder.*

strictions. There exists an external library [34] that can be used to take eddy currents into account with MuMax3, but in this work, this library was not used. The lack of structural disorder in the simulations is expected to reduce the simulated losses. In a study on magnetic friction, the losses in thin magnetic tapes were found to increase already with small introduced structural disorders [35]. Additionally, possible contributions coming from DWs are neglected. This should not have a significant effect because it is assumed that the losses due to magnetization rotations in domains dominate over DW processes at high frequencies.

When a DW is simulated, the simulation approach has to be changed. Now, quite a large area has to be simulated on the tape surface to include all the DW activity. Combining this with trying to simulate the entire tape thickness, the simulation size becomes too large. The adopted solution to this problem was to simulate different tape thicknesses. The idea is to extrapolate the results to the actual thickness by gradually increasing the simulated thickness. Despite the varying simulated tape thicknesses, material parameters of $Co_{71}Fe_4B_{15}Si_{10}$ and a constant α_G are used consistently in the DW simulations. It needs to be noted that the simulated DW regions are very small, less than 1% of the assumed domain volume. In this simulation case, PBCs can be used in the direction of the material anisotropy. Apart from the DW, small parts of the surrounding domains are also simulated. The surrounding domain areas are only a small part of the actual
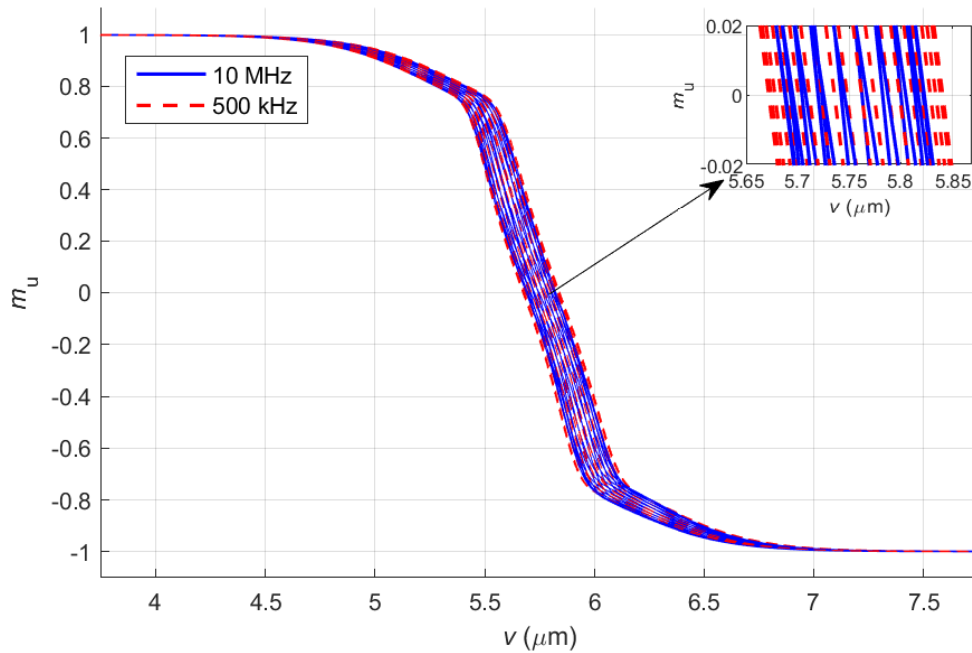
Figure 5.2. *Simulated DW motion during one period of an external field with amplitude of* $5\,\mathrm{mT}$ *and frequencies of* $10\,\mathrm{MHz}$ *and* $500\,\mathrm{kHz}$. *Particularly the inset presents how the DW motion decreases with increasing frequency. Each line represents the averaged magnetization profile of* m_u *at a certain time. The coordinate system is chosen as in Figure 3.3, and material parameters of* $Co_{71}Fe_4B_{15}Si_{10}$ *are used.*

domains, and effectively the assumption is made that only these nearest parts of the domains determine the behavior of the DW.

Figure 5.2 shows the motion of a DW during one period of an externally applied field with two different frequencies. It can be seen that with the simulated frequencies, the DW motion decreases as the frequency of the external field is increased. This observation is in agreement with the considerations on DW movement in Chapter 3. When analyzing the simulation results, it was noted that the DW magnetization profile varies on different layers along the thickness of the tape. In order to simplify the presented figure, the DW is presented in every time instance with its averaged magnetization profile. In this way, the motion can be better observed compared to drawing all the magnetization profiles. The simulated region was approximately $12\,\mu\mathrm{m}$ wide around the DW in the v-direction, and the tape thickness was approximately $1.0\,\mu\mathrm{m}$.

From the perspective of loss modeling, the DW simulations were not successful. The losses were also calculated using (4.9) in the DW simulations. The resulting losses obtained through extrapolation were several magnitudes bigger than the losses of a uniform magnetization. The DW losses were expected to be several magnitudes smaller than the domain region losses [2, 14]. Consequently, calculation of the combined losses was not attempted because it would have been entirely dominated by the DW loss and resulted in

total losses magnitudes bigger than the measured results. Most likely, the reason for the inaccurate DW losses lies in the used modeling approach. A simple linear extrapolation of the loss to the actual thickness might not be feasible. Also, the long-range interactions of the DW with the other DWs and domains cannot probably be neglected.

As a separate notion, special attention should be paid to the time over which the system is simulated. It was noted that with MuMax3, several periods of excitation were required before a steady state was achieved, and sometimes this amounted to tens of periods. As a final point on 3D micromagnetic simulations, a brief comment is made about the workflow when doing simulations with MuMax3. Doing these simulations is time-consuming due to the computational burden and the steps apart from the simulation itself. These steps include preparing the simulation input files and post-processing the results, which are often done in different programs. Consequently, creating an automated simulation environment is complicated and time-consuming, and often, as in this work, there remains some unnecessary manual work in the workflow. Though not used in this work, one possibility to improve the simulation process could be the Ubermag project which aims to bring the whole workflow into one computational environment [36].

5.2 1D micromagnetic model with eddy currents

The results calculated from (4.16) will be compared to the results of the 1D time-harmonic model and the results of a similar 1D FE model [2]. The 1D FE model is conceptually very close to the derived 1DMMEC model. The main difference between these models is that the 1D FE model uses 1D FEA to solve the distribution $b(w)$ over the thickness of the tape, whereas the 1DMMEC model utilizes the cosine series approximation. An advantage of the 1DMMEC model is the possibility to use b_0 instead of h_s as the model input. Often, it is interesting to examine the losses as a function of the magnetic flux density.

Because of having only minor differences between the 1D models, a good agreement of the calculated losses is expected. This will be presented in this section mostly for the sake of validation of the 1DMMEC model. Also, the effects of some newly introduced simulation parameters, such as the number of cosine series terms N_b and the quantities of the modified magnetostatic field calculation, are studied in order to see the effect of these parameters to the model outputs.

Figure 5.3 shows the losses as a function of frequency calculated with the 1DMMEC, the 1D FE and the 1D time-harmonic model. After solving h_s from (4.16), the losses are calculated with (3.4) when using the 1DMMEC model. A good agreement between the developed model and the other models is observed. The simulations were carried out for a 17 µm thick tape of $Co_{71}Fe_4B_{15}Si_{10}$ with a LLG damping parameter value $\alpha_G = 0.2$ [2].

When the effect of N_b to the predicted losses was examined, a trend of increasing losses
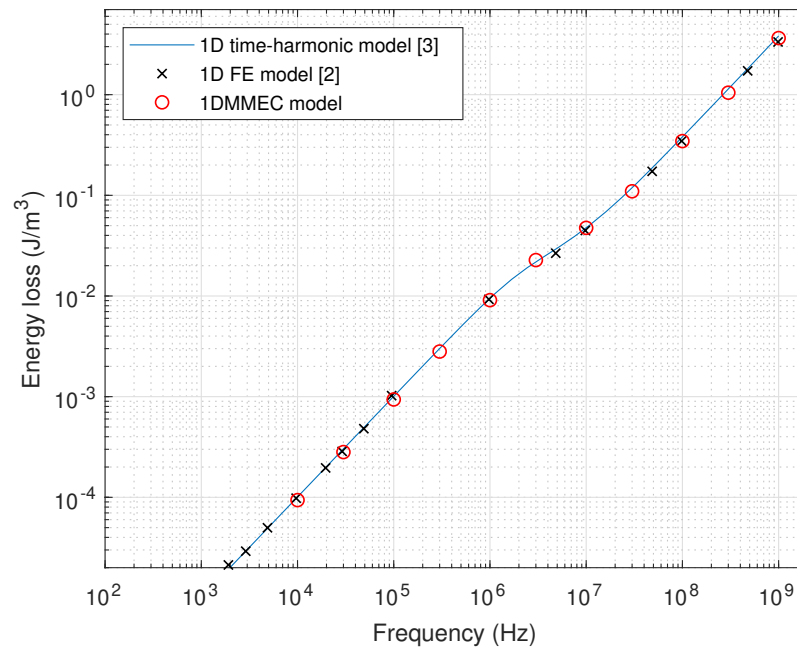
Figure 5.3. *Simulated losses as a function of frequency for a* $17\,\mu m$ *thick tape of* $Co_{71}Fe_4B_{15}Si_{10}$. *The losses predicted by the developed 1DMMEC model are in good agreement with the 1D FE model and the 1D time-harmonic model. The simulations were carried out with an applied field amplitude of* $5\,mT$.

with increasing N_b was observed. Saturating effect of the losses is observed with higher values of N_b. The saturation can be roughly said to begin with N_b values higher than 20. The value $N_b = 20$ was used in the simulated results in this section. When the parameters related to the calculation of $\boldsymbol{H}_{ms}$ were examined, the emphasis was on the number of domains N. The effect of domain width changes was not examined in this work. Also, as a function of N, the losses saturate with increasing N. However, this time the losses decrease when N is increased. A dependency of the saturation on the external field frequency was observed. Approximately $N = 20$ is enough to achieve saturation in the gigahertz range, whereas, with tens of megahertz, a value up to $N = 100$ is required. A similar dependency from frequency was not found when examining the effect of N_b. In the simulated results, a value of $N = 100$ was used.

5.3 Coupled 1D micromagnetic – 2D FE model

In order to perform calculations with the 1DMMEC–2DFE model, the 2D finite element mesh needs to be chosen. The entire cross-section of the tape wound core does not have to be modeled, but instead, a small sector of the core is enough because of the circular symmetry of the geometry. In this work, the calculations were carried out for a sector corresponding to an angle of approximately $5°$. Figure 5.4 presents the mesh that was used. The core region was set to the width of 10 tape layers and an outer diameter of
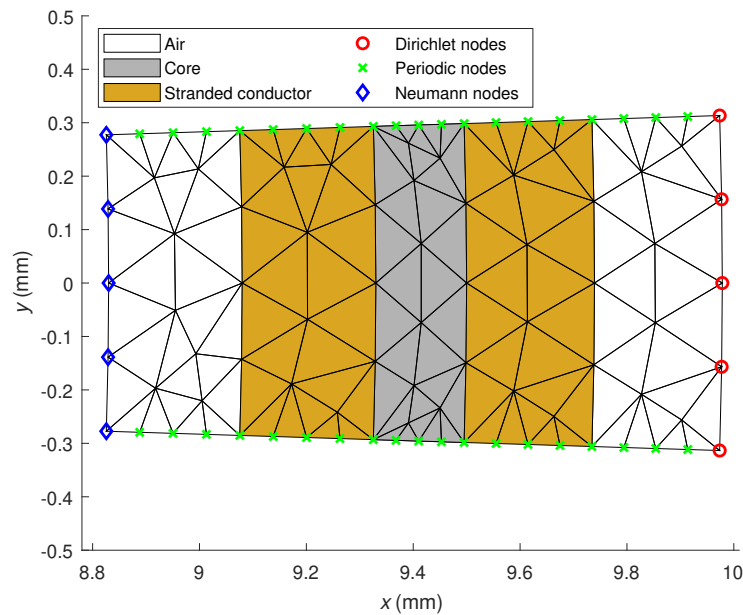
Figure 5.4. *The used mesh of the cross-section of the toroidal inductor with a tape wound core. Only a small sector of the geometry is modeled because of symmetry considerations, and a coarse mesh in a small modeled area reduces the computational burden significantly. The mesh contains 93 nodes and 136 linear elements.*

19 mm. Using quite a coarse mesh reduces the computational burden of the calculation.

The conductors of the inductor are modeled as a solid stranded conductor, meaning that eddy current effects are neglected in the conductor region. Effectively, this emulates a tightly wound inductor with thin conductors. The resulting B is almost entirely contained in the core, and only small regions of surrounding air have to be modeled. Suitable boundary conditions are imposed on the edge nodes of the mesh. On the sides of the sector, periodic boundary conditions ensure that the solution has circular symmetry. A homogeneous Neumann boundary condition is used along the inner radius, and a Dirichlet boundary condition sets all A_m to 0 along the outer radius.

Figure 5.5 shows the comparison between the losses predicted by the 1DMMEC–2DFE model, the 1D FE model, and measurements for 17 μm thick $Co_{71}Fe_4B_{15}Si_{10}$ [2]. Based on Figure 5.3, the choice of which 1D model is used in the comparison is arbitrary. When calculating the losses with the 1DMMEC–2DFE model, (3.4) is evaluated in x and y-directions of the 2D plane, and the contributions are summed to obtain the total losses. A good agreement between all the plotted losses is observed. The 1DMMEC–2DFE model can predict the losses more accurately than the 1D FE model at high frequencies. When the frequency is lowered, the model predictions coincide and begin to describe the measured losses less accurately. This is because the assumption to neglect p_{dw} is no more valid at low frequencies.
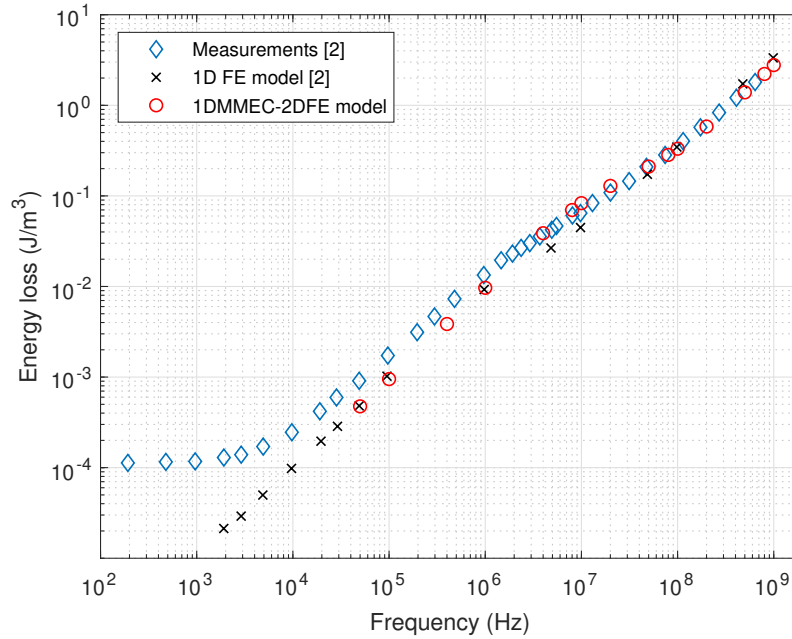
Figure 5.5. *Losses as function of frequency for* $17\,\mu m$ *thick* $Co_{71}Fe_4B_{15}Si_{10}$*. The amplitude of the applied field is* $5\,mT$*. The losses predicted by the 1DMMEC-2DFE model and the 1D FE model are compared to measurements. Both the models are in good agreement with the measurements, the performance of the 1DMMEC–2DFE model being slightly better at frequencies higher than* $1\,MHz$*. At lower frequencies, the models predict similar losses.*

Despite the good results in Figure 5.5, some discussion is needed on the chosen simulation parameters. Now the losses decrease as a function of N_{b} and saturate quicker when compared to the 1DMMEC model. The value $N_{\mathrm{b}} = 3$ was used in the simulations. The losses were observed to have a similar dependency of N in the calculation of $\boldsymbol{H}_{\mathrm{ms}}$ as with the 1DMMEC model, and the value $N = 100$ was used.

A surprisingly strong effect of Δt was observed. Figure 5.6 presents how the predicted losses vary in the 1DMMEC–2DFE model with different values of Δt. In the worst case, the losses differ by multiples when simulations with $\Delta t = 0.2\,\mathrm{ps}$ and $\Delta t = 2\,\mathrm{ps}$ are compared. The losses are consistently higher with a larger timestep. With lower frequencies, the dependency on Δt decreases. This feature was already used in Figure 5.5 to reduce the computational burden of simulations with lower frequencies. Simulations with frequencies higher than $5\,\mathrm{MHz}$ were carried out with $\Delta t = 0.1\,\mathrm{ps}$, whereas with lower frequencies $\Delta t = 2\,\mathrm{ps}$ was used. A similar dependency of Δt was not observed with the 1DMMEC model. The described behavior of the model with different values of Δt may indicate a problem in the modeling approach and should be studied further. Another possible cause is a bug in the code implementation.

In the simulations with the 1DMMEC–2DFE model, a relatively low value $\alpha_{\mathrm{G}} = 0.04$ was chosen. For comparison, the value was $\alpha_{\mathrm{G}} = 0.2$ in the 1D simulations of the previous
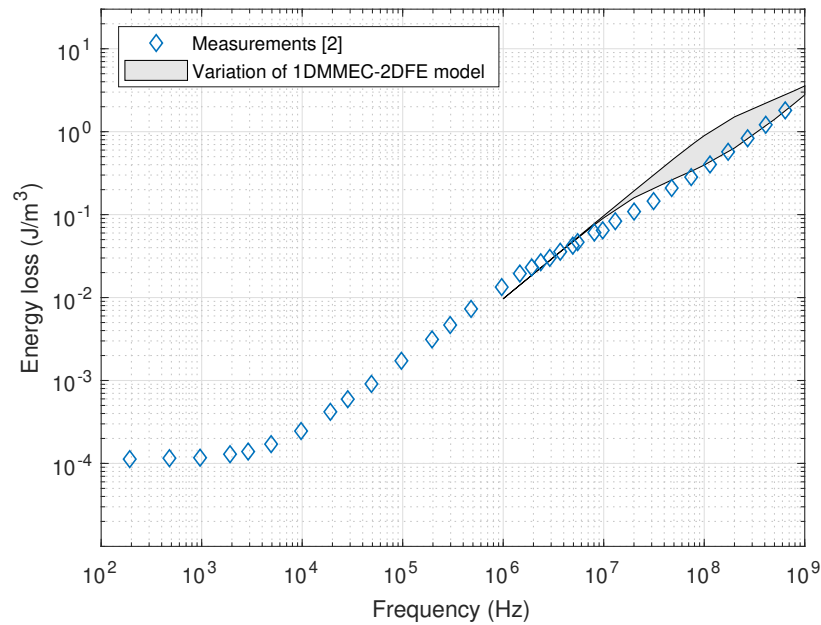
Figure 5.6. *The dependency of losses on Δt for $17\,\mu m$ thick $Co_{71}Fe_4B_{15}Si_{10}$. The difference in the predicted losses with Δt values $0.2\,ps$ and $2\,ps$ is highlighted in the figure. Using a smaller Δt leads to better agreement with the measured losses. The amplitude of the applied field is $5\,mT$*

section. The predicted losses increase as a function of α_G, meaning that with higher values than $\alpha_G = 0.04$ the 1DMMEC–2DFE model would give higher losses than the measurements. Different values of the damping parameter are used in the literature. In [2], α_G varies between $0.15 - 0.22$ and the analysis of [25] suggests $\alpha_G \sim 0.1 - 0.2$, both for Co-based alloys. In both of these studies, α_G is assumed to increase as a function of the material thickness. For $20\,\mu m$ thick FINEMET ring samples, [3] uses the value $\alpha_G = 0.04$ and [37] $\alpha_G = 0.06$. To some extent, α_G can be seen as a fitting parameter for which the previous works give an order of magnitude. Unconventional choice of α_G can also lead to overfitting which might hide model inaccuracies.

In order to test for possible overfitting, the losses are also calculated for different materials than $17\,\mu m$ thick $Co_{71}Fe_4B_{15}Si_{10}$. The simulation parameters are mostly kept the same apart from some changes in the material parameters. Figure 5.7 shows the calculated losses for $6.1\,\mu m$ and $13\,\mu m$ thick $Co_{67}Fe_4B_{14.5}Si_{14.5}$, and Figure 5.8 for $20\,\mu m$ thick $Co_{67}Fe_4B_{14.5}Si_{14.5}$ with material parameters from [2]. In the simulations $\alpha_G = 0.04$ was used. There is a fairly good agreement between the losses with all the tape thicknesses. However, the results in Figure 5.5 are clearly better. Additionally, the better accuracy of the $13\,\mu m$ and $20\,\mu m$ thick tapes compared to the $6.1\,\mu m$ tape leads to the conclusion that with these parameters the 1DMMEC–2DFE model works the better the closer the tape thickness is to $17\,\mu m$. A possible explanation to this is that α_G was kept constant despite changing the tape thicknesses. However, in order to obtain higher losses in the $6.1\,\mu m$
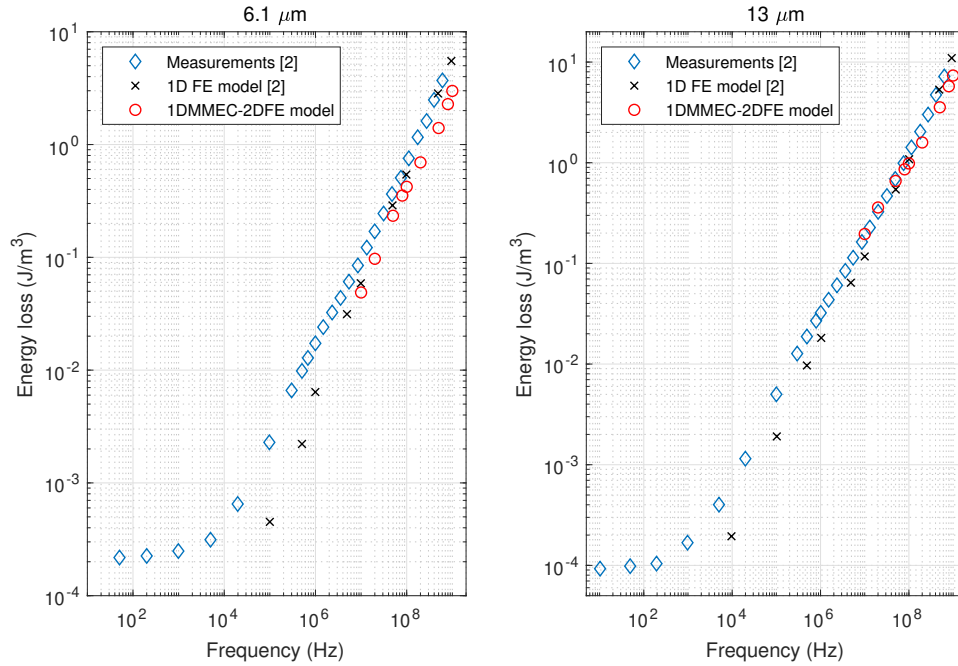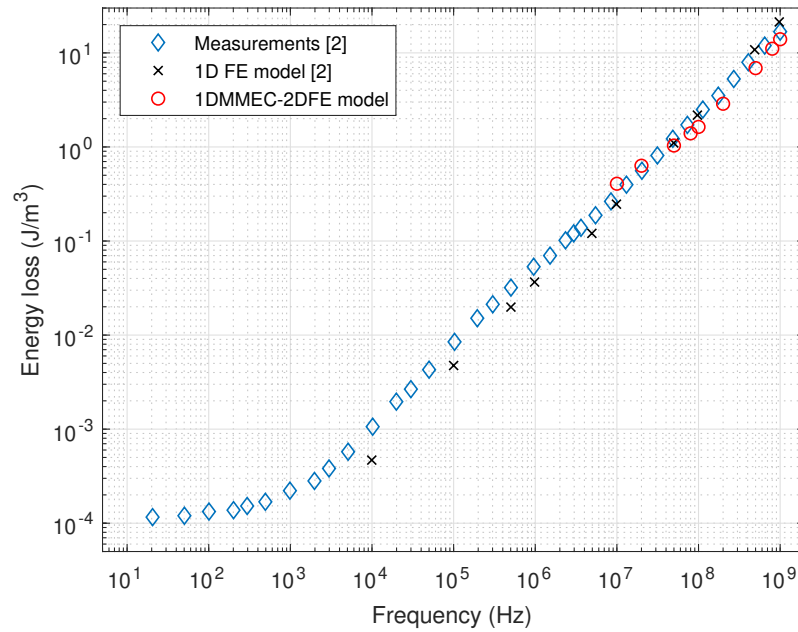
Figure 5.7. *Losses as function of frequency for* $6.1\,\mu$m *(left) and* $13\,\mu$m *(right) thick* $Co_{67}Fe_4B_{14.5}Si_{14.5}$. *The losses predicted by the 1DMMEC–2DFE model and the 1D FE model are compared to measurements. The losses are calculated with the 1DMMEC–2DFE model starting from* $10\,$MHz *with an applied field amplitude of* $10\,$mT. *Timestep of* $\Delta t = 0.2\,$ps *was used. Different meshes had to be used due to changing core dimensions. A core with a thickness of 10 tape layers was simulated in both cases.*

case, α_G would have to be increased which contradicts the notion of increasing α_G as a function of thickness presented in [2] and [25].

The 1DMMEC–2DFE model can also be used to determine the hysteresis loop for the cross-section of the tape wound core. Spatial averages of the relevant field quantities are required in order to be able to plot single loops. The mean value of the tangential magnetic flux density $B_{0,\mathrm{tan}}$ can be directly averaged over the cross-section of the core. Averaged $H_{s,0,\mathrm{tan}}$ is obtained through a spatially averaged *magnetomotive force*, similarly to what is done in [38]. The spatially averaged field quantities are denoted as $\langle B_{0,\mathrm{tan}} \rangle$ and $\langle H_{s,0,\mathrm{tan}} \rangle$. Figure 5.9 presents examples of hysteresis loops under applied field frequencies of $10\,$MHz and $100\,$MHz. The simulations were carried out with the mesh of Figure 5.4 and with the same parameters as in Figure 5.5. The increasing area of the hysteresis loop as a function of frequency demonstrates the increasing losses with higher frequencies.

Examining the fields obtained by solving the 1DMMEC–2DFE model allows us to check on some previously made assumptions. The reluctivity of free space ν_0 was used as the material property in the radial direction with the assumption that radial components of the fields are small. Also, the higher-order terms in the cosine series of $\boldsymbol{H}_s$ are expected to

Figure 5.8. *Comparison of losses as function of frequency for* $20\,\mu m$ *thick* $Co_{67}Fe_4B_{14.5}Si_{14.5}$. *The losses are calculated with the 1DMMEC–2DFE model starting from* $10\,MHz$ *with an applied field amplitude of* $10\,mT$. *As in Figure 5.7, timestep of* $\Delta t = 0.2\,ps$ *was used and the calculations were carried out for a core with a thickness of 10 tape layers.*
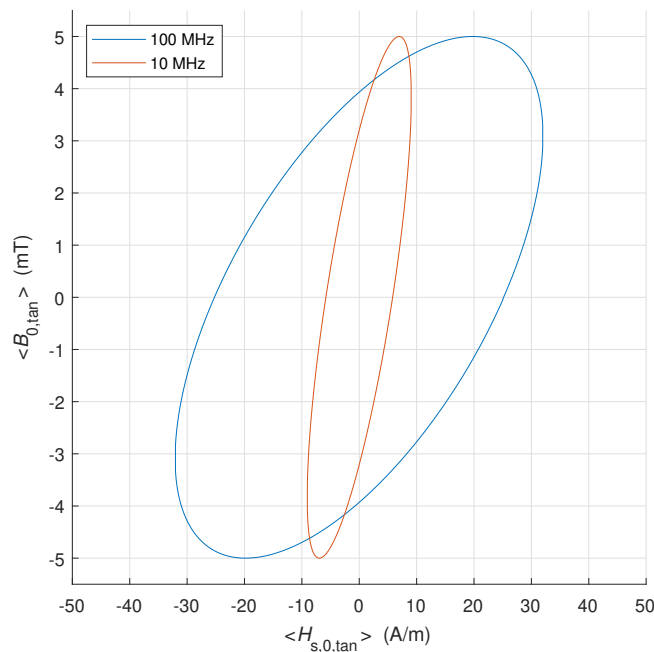
Figure 5.9. *Hysteresis loops predicted by the 1DMMEC–2DFE model. The spatially averaged fields* $\langle B_{0,\mathrm{tan}} \rangle$ *and* $\langle H_{s,0,\mathrm{tan}} \rangle$ *produce one hysteresis loop for the entire geometry. The simulations were carried out for* $17\,\mu m$ *thick* $Co_{71}Fe_4B_{15}Si_{10}$ *under applied sinusoidal external field with an amplitude of* $5\,mT$ *and frequencies of* $100\,MHz$ *and* $10\,MHz$.
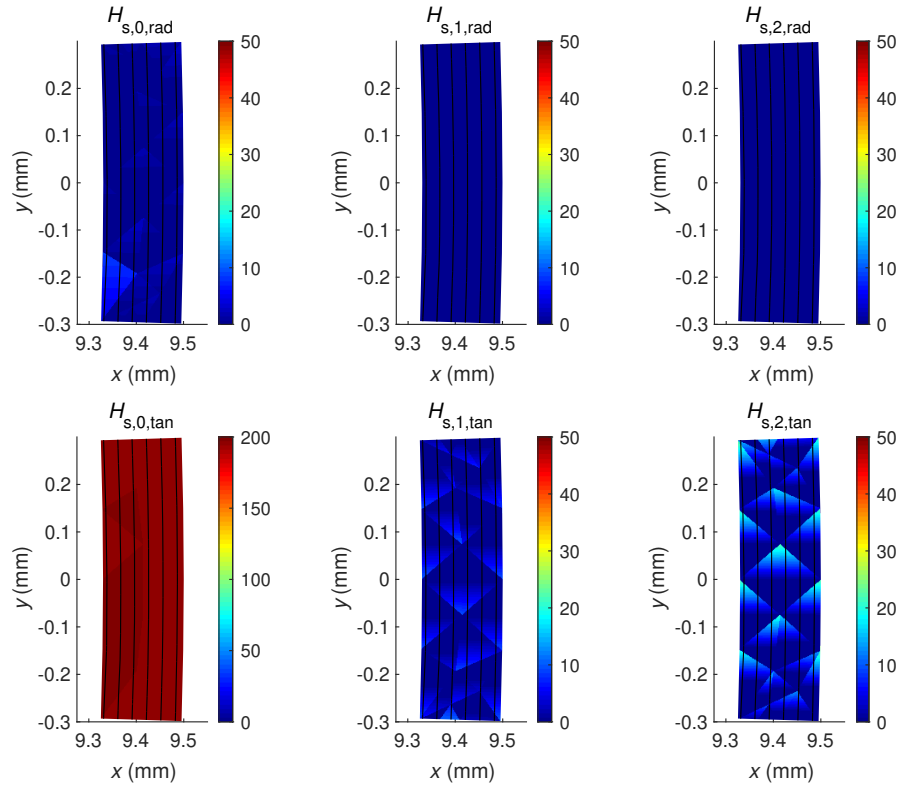
Figure 5.10. *Magnitudes of the different cosine series terms of $\boldsymbol{H}_\mathrm{s}$ over the core geometry. The unit on the color bars is $\mathrm{A/m}$. The simulation was carried out for $17\,\mu\mathrm{m}$ thick $Co_{71}Fe_4B_{15}Si_{10}$. As assumed, $H_{\mathrm{s},0,\mathrm{tan}}$ dominates over the other terms. Note the varying upper limit of the color bars. The vertical lines plotted in the core are not the tape layers but the contours of the fields.*

be 0, a property originating from (3.7). A simulation was carried out with $N_\mathrm{b} = 3$, and Figure 5.10 shows instantaneous magnitudes of all the different cosine series terms of $\boldsymbol{H}_\mathrm{s}$ over the core geometry. As assumed, $H_{\mathrm{s},0,\mathrm{tan}}$ dominates over all the other terms. Small $H_{\mathrm{s},0,\mathrm{rad}}$ indicates that the radial effects are small, and the assumption of zero-valued higher-order terms is reasonably well satisfied. The relatively small deviation from zero with the other terms can be considered numerical error dependent on the number of elements in the mesh. A denser mesh is expected to reduce the magnitudes of the higher-order terms.

As a final point, the computational performance of the 1DMMEC–2DFE model is discussed. Throughout the derivation of the model, simplifying assumptions have been made to reduce the computational burden. These assumptions are necessary because the 3D micromagnetic simulations proved that general micromagnetic simulations in large systems are not computationally feasible. To briefly recap these assumptions: a simple $\boldsymbol{M}$ neglecting the DW processes was assumed in the tape, which reduced the micromagnetic description to 1D over the thickness of the tape. The cosine series approximation for the eddy current problem was evaluated with only a few terms with the 1DMMEC–

2DFE model and the $\boldsymbol{H}_{\mathrm{ms}}$ calculation was simplified. Modifications were done to the cross-section geometry, and homogenization was utilized to allow for a coarser mesh. Additionally, only a small sector of the geometry was modeled, and the radial field quantities were expressed with a simple constitutive law.

The remaining computational burden can be examined through the time required to compute one timestep and the total number of timesteps in the simulation. The calculation of a single timestep is quite fast. Even with a single core of old hardware (Intel Core i5-4300U), the time required for one step is on average 15 ms when $N_{\mathrm{b}} = 3$ and mesh of Figure 5.4 are used. If the Newton-Raphson iteration would be removed from the code implementation, a speed-up by approximately the factor 2 is expected. Parallelization of the computation is not expected to significantly accelerate the calculation of individual timesteps.

The total number of timesteps required increases at lower frequencies. This is further amplified by the need to use also from the perspective of micromagnetics small Δt as was demonstrated in Figure 5.6. The possibility to increase Δt at low frequencies helps to some extent, but this idea was not studied for values over $\Delta t = 2\,\mathrm{ps}$. Even with $\Delta t = 2\,\mathrm{ps}$, at $f = 50\,\mathrm{kHz}$ simulation over 3 periods requires 30 million timesteps. The sheer number of timesteps at low frequencies makes the calculation slow. On the other hand, the calculation times remain reasonable at high frequencies. As each timestep depends on the values of the previous timestep, parallelization of the calculation is difficult. The computation was observed to scale linearly with an increasing number of timesteps when an adequate amount of memory was available.

6 CONCLUSION

This thesis is concluded by summarizing the results obtained from the different modeling approaches. The developed models for tape wound magnetic cores: the 1DMMEC model and the 1DMMEC–2DFE model, are emphasized. Suggestions for future work on the topic are made based on the obtained results.

6.1 Discussion on the results

The 3D micromagnetic simulations with MuMax3 could not be utilized to model the iron losses of tape wound cores accurately. The computational burden of these simulations makes it impossible to directly simulate a piece of tape large enough to include all the magnetization processes. An attempt to simulate domains and DWs separately and combine their contributions did not give satisfactory results. Simulations carried out with MuMax3 proved to be more insightful with systems of smaller size than individual domains in the tape. Simulations of a single DW could be used to observe the reducing DW motion with higher excitation frequencies.

The 1DMMEC model introduces a micromagnetic model which approximates the solution of the eddy current problem over the tape thickness in terms of a cosine series. Contrary to existing models, the model input is the magnetic flux density. The predicted iron losses are in good agreement with models already presented in the literature. The developed model introduces some new parameters through the cosine series approximation and the magnetostatic field H_{ms} calculation whose roles in the predicted losses were studied. The 1DMMEC model and the reference models are all derived for a single strip of tape and do not take into account the geometry of tape wound cores.

The 1DMMEC–2DFE model couples the 1DMMEC model to 2D FEM. The combined model utilizes a micromagnetic description for the tape material over the entire cross-section of the core. The losses predicted with this model show good agreement with measured iron losses. The model shows even potential to predict the measurements more accurately than the previously mentioned models derived for a single strip of tape. The accuracy of the predicted losses decreases slightly when the thickness of the tape is decreased. On the other hand, the simulation parameters were not modified to achieve the best fit with the measured losses in every situation.

The 1DMMEC–2DFE model simulations were planned carefully to manage and reduce the computational burden. The solution of the system is fast in individual time steps. However, the large number of time steps at low excitation frequencies makes the calculation slow. The unexpectedly strong dependency on the timestep length Δt further increases the computational burden because small values of Δt have to be used.

6.2 Suggestions for future work

Based on the results presented in this thesis, the 1DMMEC–2DFE model has been shown to predict iron losses highly accurately in some cases. Future work could concentrate on showing that the model accuracy applies more generally. In order to achieve this, the role of some model parameters could be investigated further.

The role and suitable values of the LLG-equation damping parameter α_{G} could be studied. It was noted that when moving from the 1DMMEC model to the 1DMMEC–2DFE model, the value of α_{G} needs to be reduced significantly. It is not clear whether the geometry of the system can affect the value of α_{G}. If α_{G} would be used as a fitting parameter, an increasing α_{G} with thinner tape thicknesses would have to be used to fit better the iron losses presented in this work. However, this contradicts some literature where increasing α_{G} with thicker tapes is suggested.

The approximate calculation of $\boldsymbol{H}_{\mathrm{ms}}$ could be improved. A method that better considers the geometry of tape wound cores is expected to improve the description of the system. On the other hand, more accurate evaluation of $\boldsymbol{H}_{\mathrm{ms}}$ can increase the computational burden of the model. The suitable amount of domains and tape layers which are taken into account in evaluating $\boldsymbol{H}_{\mathrm{ms}}$ would have to be determined for the improved method.

There are multiple possibilities to reduce the computational burden of the 1DMMEC–2DFE model. Further study on the time step length Δt can help find optimal values for smaller frequencies. Also, changing the forward Euler discretization to a method with better convergence properties could allow increasing Δt. Modifying the code implementation to remove the unnecessary Newton-Raphson iteration is expected to reduce the computational burden to some extent. One interesting alternative would be to attempt a time-harmonic approach over the tape wound core cross-section. The computational performance of such a model would be superior to time-domain methods.

REFERENCES

[1]   Wang, F. F. and Zhang, Z. Overview of silicon carbide technology: Device, converter, system, and application. *CPSS Transactions on Power Electronics and Applications* 1.1 (2016), 13–32.

[2]   Bottauscio, O., Fiorillo, F., Beatrice, C., Caprile, A. and Magni, A. Modeling High-Frequency Magnetic Losses in Transverse Anisotropy Amorphous Ribbons. *IEEE Transactions on Magnetics* 51.3 (2015).

[3]   Beatrice, C., Dobák, S., Ferrara, E., Fiorillo, F., Ragusa, C., Füzer, J. and Kollár, P. Broadband magnetic losses of nanocrystalline ribbons and powder cores. *Journal of Magnetism and Magnetic Materials* 420 (2016), 317–323.

[4]   Bertotti, G. *Hysteresis in magnetism : for physicists, materials scientists, and engineers*. San Diego: Academic Press, 1998.

[5]   Hubert, A. and Schäfer, R. *Magnetic Domains: The Analysis of Magnetic Microstructures*. Springer Berlin / Heidelberg, 2008.

[6]   Jackson, J. D. *Classical electrodynamics*. 3rd ed. Wiley, 1999.

[7]   Pulse, Power & Measurement Ltd. [Online; accessed 15.2.2022]. URL: `https://ppmpower.co.uk/products/magnetic-components/magnetic-cores/`.

[8]   Herzer, G. Nanocrystalline soft magnetic alloys. *Handbook of Magnetic Materials* 10 (1997), 415–462.

[9]   Yoshizawa, Y. and Yamauchi, K. Effects of magnetic field annealing on magnetic properties in ultrafine crystalline Fe-Cu-Nb-Si-B alloys. *IEEE Transactions on Magnetics* 25.5 (1989), 3324–3326.

[10]   Goldman, A. *Magnetic Components for Power Electronics*. Boston, MA: Springer US, 2002.

[11]   Petzold, J. Applications of nanocrystalline softmagnetic materials for modern electronic devices. *Scripta Materialia* 48.7 (2003), 895–901.

[12]   Flohrer, S., Schäfer, R., McCord, J., Roth, S., Schultz, L., Fiorillo, F., Günther, W. and Herzer, G. Dynamic magnetization process of nanocrystalline tape wound cores with transverse field-induced anisotropy. *Acta Materialia* 54.18 (2006), 4693–4698.

[13]   Magni, A., Fiorillo, F., Caprile, A., Ferrara, E. and Martino, L. Fluxmetric-magneto optical approach to broadband energy losses in amorphous ribbons. *Journal of Applied Physics* 109.7 (2011), 07A322.

[14] Magni, A., Fiorillo, F., Ferrara, E., Caprile, A., Bottauscio, O. and Beatrice, C. Domain Wall Processes, Rotations, and High-Frequency Losses in Thin Laminations. *IEEE Transactions on Magnetics* 48.11 (2012), 3796–3799.

[15] Magni, A., Beatrice, C., Bottauscio, O., Caprile, A., Ferrara, E. and Fiorillo, F. Magnetization Process in Thin Laminations up to 1 GHz. *IEEE Transactions on Magnetics* 48.4 (2012), 1363–1366.

[16] Fiorillo, F., Ferrara, E., Coïsson, M., Beatrice, C. and Banu, N. Magnetic properties of soft ferrites and amorphous ribbons up to radiofrequencies. *Journal of Magnetism and Magnetic Materials* 322.9 (2010). Proceedings of the Joint European Magnetic Symposia, 1497–1504.

[17] Atallah, K. and Howe, D. Calculation of the rotational power loss in electrical steel laminations from measured H and B. *IEEE Transactions on Magnetics* 29.6 (1993), 3547–3549.

[18] Rasilo, P., Dlala, E., Fonteyn, K., Pippuri, J., Belahcen, A. and Arkkio, A. Model of laminated ferromagnetic cores for loss prediction in electrical machines. *IET Electric Power Applications* 5 (Aug. 2011), 580–588.

[19] Brown, W. F. *Micromagnetics*. 18. Interscience Tracts on Physics and Astronomy. Interscience publishers, 1963.

[20] Kronmüller, H. General Micromagnetic Theory. *Handbook of Magnetism and Advanced Magnetic Materials*. 2007.

[21] Van de Wiele, B. Numerical study of magnetic processes: extending the Landau-Lifshitz-Gilbert approach from nanoscale to microscale. PhD thesis. Ghent University, 2010, p. 273.

[22] Azzawi, S., Hindmarch, A. T. and Atkinson, D. Magnetic damping phenomena in ferromagnetic thin-films and multilayers. *Journal of Physics D: Applied Physics* 50.47 (2017), 473001.

[23] Donahue, M. and Porter, D. Exchange energy formulations for 3D micromagnetics. *Physica B: Condensed Matter* 343.1 (2004). Proceedings of the Fourth Intional Conference on Hysteresis and Micromagnetic Modeling, 177–183.

[24] Aharoni, A. Demagnetizing factors for rectangular ferromagnetic prisms. *Journal of Applied Physics* 83.6 (1998), 3432–3434.

[25] Magni, A., Bottauscio, O., Caprile, A., Celegato, F., Ferrara, E. and Fiorillo, F. Spin precession by pulsed inductive magnetometry in thin amorphous plates. *Journal of Applied Physics* 115.17 (2014), 17A338.

[26] Miltat, J. E. and Donahue, M. J. Numerical Micromagnetics: Finite Difference Methods. *Handbook of Magnetism and Advanced Magnetic Materials* (2007).

[27] Bottauscio, O. and Manzin, A. Efficiency of the Geometric Integration of Landau–Lifshitz–Gilbert Equation Based on Cayley Transform. *IEEE Transactions on Magnetics* 47.5 (2011), 1154–1157.

[28] Vansteenkiste, A., Leliaert, J., Dvornik, M., Helsen, M., Garcia-Sanchez, F. and Van Waeyenberge, B. The design and verification of MuMax3. *AIP Advances* 4.10 (2014), 107133.

[29] Rissanen, I. and Laurson, L. Magnetic non-contact friction from domain wall dynamics actuated by oscillatory mechanical motion. *Journal of Physics D: Applied Physics* 52.44 (2019), 445002.

[30] Zienkiewicz, O. C. and Taylor, R. L. *The Finite Element Method, Vol. 1*. 5th ed. Butterworth-Heinemann, 2000.

[31] Luomi, J. *Finite element methods for electrical machines*. Lecture notes. 1993.

[32] Gyselinck, J., Sabariego, R. and Dular, P. A nonlinear time-domain homogenization technique for laminated iron cores in three-dimensional finite-element models. *IEEE Transactions on Magnetics* 42.4 (2006), 763–766.

[33] Tsukerman, I., Konrad, A. and Lavers, J. A method for circuit connections in time-dependent eddy current problems. *IEEE transactions on magnetics* 28.2 (1992), 1299–1302.

[34] Rissanen, I. and Laurson, L. Moving magnets in a micromagnetic finite-difference framework. *Phys. Rev. E* 97 (5 2018), 053301.

[35] Rissanen, I. and Laurson, L. Bursty magnetic friction between polycrystalline thin films with domain walls. *Physical review. B* 100.14 (2019).

[36] Beg, M., Lang, M. and Fangohr, H. Ubermag: Towards more effective micromagnetic workflows. *IEEE Transactions on Magnetics* 58.2 (2022), 1–5.

[37] Ferrara, E., Fiorillo, F., Beatrice, C., Dobák, S., Ragusa, C., Magni, A. and Appino, C. Characterization and assessment of the wideband magnetic properties of nanocrystalline alloys and soft ferrites. *Journal of materials research* 33.15 (2018), 2120–2137.

[38] Gürbüz, I. T., Rasilo, P., Martin, F., Aydin, U., Osemwinyen, O., Ali, A. B. A., Chamosa, M. and Belahcen, A. Finite-Element Modeling and Characterization of Iron Losses in 12 mm Thick Steel Laminations Including the Effect of Cutting. *IEEE Access* 9 (2021), 115710–115718.

A CALCULATION OF THE GEOMETRY DEPENDENCY OF THE MAGNETOSTATIC FIELD

This appendix presents how the geometry dependent matrix $\boldsymbol{N}$ of (4.6) is obtained. In other words, the steps between (4.6) and (4.7) are presented. To recap, (4.6) expresses the magnetostatic field as

$$\boldsymbol{H}_{\mathrm{ms}}(\boldsymbol{w}_0) = \frac{1}{4\pi} \sum_{n=-N}^{N} \int_{S_n} (\hat{\boldsymbol{e}}_{\mathrm{n}} \cdot \boldsymbol{M}) \frac{\boldsymbol{w}_0 - \boldsymbol{r}'}{\|\boldsymbol{w}_0 - \boldsymbol{r}'\|^3} d\boldsymbol{a}'. \tag{A.1}$$

In order to evaluate the surface integral term, a coordinate system needs to be chosen. The coordinates are chosen as in Figure 3.3 and the origin is set to the center of a domain. The surface of the domain consists of 6 rectangles named after the coordinate which stays constant as u^+, u^-, v^+, v^-, w^+ and w^-. The dimensions of the domain are denoted as Δu, Δv and Δw. The magnetostatic field is evaluated along the w-axis at point $\boldsymbol{w}_0 = \begin{bmatrix} 0 & 0 & w_0 \end{bmatrix}^{\mathrm{T}}$. Equation (A.1) can be written as

$$\begin{aligned}
\boldsymbol{H}_{\mathrm{ms}}(\boldsymbol{w}_0) = \frac{1}{4\pi} \sum_{n=-N}^{N} & M_{\mathrm{u}} \int_{u_n^+} \frac{\boldsymbol{w}_0 - \boldsymbol{r}'}{\|\boldsymbol{w}_0 - \boldsymbol{r}'\|^3} d\boldsymbol{a}' - M_{\mathrm{u}} \int_{u_n^-} \frac{\boldsymbol{w}_0 - \boldsymbol{r}'}{\|\boldsymbol{w}_0 - \boldsymbol{r}'\|^3} d\boldsymbol{a}' \\
& + M_{\mathrm{v}} \int_{v_n^+} \frac{\boldsymbol{w}_0 - \boldsymbol{r}'}{\|\boldsymbol{w}_0 - \boldsymbol{r}'\|^3} d\boldsymbol{a}' - M_{\mathrm{v}} \int_{v_n^-} \frac{\boldsymbol{w}_0 - \boldsymbol{r}'}{\|\boldsymbol{w}_0 - \boldsymbol{r}'\|^3} d\boldsymbol{a}' \\
& + M_{\mathrm{w}} \int_{w_n^+} \frac{\boldsymbol{w}_0 - \boldsymbol{r}'}{\|\boldsymbol{w}_0 - \boldsymbol{r}'\|^3} d\boldsymbol{a}' - M_{\mathrm{w}} \int_{w_n^-} \frac{\boldsymbol{w}_0 - \boldsymbol{r}'}{\|\boldsymbol{w}_0 - \boldsymbol{r}'\|^3} d\boldsymbol{a}',
\end{aligned} \tag{A.2}$$

which can be further expressed as

$$
\begin{aligned}
\boldsymbol{H}_{\mathrm{ms}}(\boldsymbol{w}_0) = \frac{1}{4\pi} \sum_{n=-N}^{N} & M_{\mathrm{u}} \int_{v_{\min,n}}^{v_{\max,n}} \int_{-\Delta w/2}^{\Delta w/2} \frac{\left[-\Delta u/2 \quad -v' \quad w_0 - w' \right]^{\mathrm{T}}}{\left\| \left[-\Delta u/2 \quad -v' \quad w_0 - w' \right]^{\mathrm{T}} \right\|^3} dw' dv' \\
& - M_{\mathrm{u}} \int_{v_{\min,n}}^{v_{\max,n}} \int_{-\Delta w/2}^{\Delta w/2} \frac{\left[\Delta u/2 \quad -v' \quad w_0 - w' \right]^{\mathrm{T}}}{\left\| \left[\Delta u/2 \quad -v' \quad w_0 - w' \right]^{\mathrm{T}} \right\|^3} dw' dv' \\
& + M_{\mathrm{v}} \int_{-\Delta u/2}^{\Delta u/2} \int_{-\Delta w/2}^{\Delta w/2} \frac{\left[-u' \quad -v_{\max,n} \quad w_0 - w' \right]^{\mathrm{T}}}{\left\| \left[-u' \quad -v_{\max,n} \quad w_0 - w' \right]^{\mathrm{T}} \right\|^3} dw' du' \\
& - M_{\mathrm{v}} \int_{-\Delta u/2}^{\Delta u/2} \int_{-\Delta w/2}^{\Delta w/2} \frac{\left[-u' \quad -v_{\min,n} \quad w_0 - w' \right]^{\mathrm{T}}}{\left\| \left[-u' \quad -v_{\min,n} \quad w_0 - w' \right]^{\mathrm{T}} \right\|^3} dw' du' \\
& + M_{\mathrm{w}} \int_{-\Delta u/2}^{\Delta u/2} \int_{v_{\min,n}}^{v_{\max,n}} \frac{\left[-u' \quad -v' \quad w_0 - \Delta w/2 \right]^{\mathrm{T}}}{\left\| \left[-u' \quad -v' \quad w_0 - \Delta w/2 \right]^{\mathrm{T}} \right\|^3} dv' du' \\
& - M_{\mathrm{w}} \int_{-\Delta u/2}^{\Delta u/2} \int_{v_{\min,n}}^{v_{\max,n}} \frac{\left[-u' \quad -v' \quad w_0 + \Delta w/2 \right]^{\mathrm{T}}}{\left\| \left[-u' \quad -v' \quad w_0 + \Delta w/2 \right]^{\mathrm{T}} \right\|^3} dv' du'.
\end{aligned}
$$

$$\text{(A.3)}$$

Equation (A.3) demonstrates the integral in all its details. Dependency on n is found in the integration limits in the v-direction, and the v-coordinate of surfaces v^+ and v^-. For every n holds that $v_{\max,n} - v_{\min,n} = \Delta v$. Also $\boldsymbol{M}$ depends on n. When the domain $n = 0$ is set to have a positive M_{u}, the u-component of the magnetization is M_{u} in domains with n even or 0 and -M_{u} with n odd. The v-component of the magnetization does not change from domain to domain, and M_{w} is assumed behave as M_{u}. Due to the length of (A.3), further simplifications are done in parts. The part proportional to M_{u} can be written as

$$\frac{1}{4\pi} \sum_{n=-N}^{N} M_{\mathrm{u}} \int_{v_{\min,n}}^{v_{\max,n}} \int_{-\Delta w/2}^{\Delta w/2} \frac{\begin{bmatrix} -\Delta u & 0 & 0 \end{bmatrix}^{\mathrm{T}}}{\left\| \begin{bmatrix} -\Delta u/2 & -v' & w_0 - w' \end{bmatrix}^{\mathrm{T}} \right\|^3} dw' dv'$$

$$= M_{\mathrm{u}} \sum_{n=-N,...,N}^{0,\mathrm{even}} \frac{1}{4\pi} \int_{v_{\min,n}}^{v_{\max,n}} \int_{-\Delta w/2}^{\Delta w/2} \frac{\begin{bmatrix} -\Delta u & 0 & 0 \end{bmatrix}^{\mathrm{T}}}{\left\| \begin{bmatrix} -\Delta u/2 & -v' & w_0 - w' \end{bmatrix}^{\mathrm{T}} \right\|^3} dw' dv'$$

$$- M_{\mathrm{u}} \sum_{n=-N,...,N}^{\mathrm{odd}} \frac{1}{4\pi} \int_{v_{\min,n}}^{v_{\max,n}} \int_{-\Delta w/2}^{\Delta w/2} \frac{\begin{bmatrix} -\Delta u & 0 & 0 \end{bmatrix}^{\mathrm{T}}}{\left\| \begin{bmatrix} -\Delta u/2 & -v' & w_0 - w' \end{bmatrix}^{\mathrm{T}} \right\|^3} dw' dv'$$

$$= M_{\mathrm{u}} \boldsymbol{N}_{\mathrm{u}}. \tag{A.4}$$

Respectively, the part proportional to M_{v} can be expressed as

$$M_{\mathrm{v}} \sum_{n=-N}^{N} \frac{1}{4\pi} \int_{-\Delta u/2}^{\Delta u/2} \int_{-\Delta w/2}^{\Delta w/2} \frac{\begin{bmatrix} -u' & -v_{\max,n} & w_0 - w' \end{bmatrix}^{\mathrm{T}}}{\left\| \begin{bmatrix} -u' & -v_{\max,n} & w_0 - w' \end{bmatrix}^{\mathrm{T}} \right\|^3}$$

$$- \frac{\begin{bmatrix} -u' & -v_{\min,n} & w_0 - w' \end{bmatrix}^{\mathrm{T}}}{\left\| \begin{bmatrix} -u' & -v_{\min,n} & w_0 - w' \end{bmatrix}^{\mathrm{T}} \right\|^3} dw' du'$$

$$= M_{\mathrm{v}} \boldsymbol{N}_{\mathrm{v}}, \tag{A.5}$$

and the part proportional to M_{w} as

$$
\begin{aligned}
& M_{\mathrm{w}} \frac{1}{4\pi} \sum_{n=-N,...,N}^{0,\text{even}} \int_{-\Delta u/2}^{\Delta u/2} \int_{v_{\min,n}}^{v_{\max,n}} \frac{\begin{bmatrix} -u' & -v' & w_0 - \Delta w/2 \end{bmatrix}^{\mathrm{T}}}{\left\| \begin{bmatrix} -u' & -v' & w_0 - \Delta w/2 \end{bmatrix}^{\mathrm{T}} \right\|^3} dv' du' \\
& \qquad - \int_{-\Delta u/2}^{\Delta u/2} \int_{v_{\min,n}}^{v_{\max,n}} \frac{\begin{bmatrix} -u' & -v' & w_0 + \Delta w/2 \end{bmatrix}^{\mathrm{T}}}{\left\| \begin{bmatrix} -u' & -v' & w_0 + \Delta w/2 \end{bmatrix}^{\mathrm{T}} \right\|^3} dv' du' \\
& -M_{\mathrm{w}} \frac{1}{4\pi} \sum_{n=-N,...,N}^{0,\text{odd}} \int_{-\Delta u/2}^{\Delta u/2} \int_{v_{\min,n}}^{v_{\max,n}} \frac{\begin{bmatrix} -u' & -v' & w_0 - \Delta w/2 \end{bmatrix}^{\mathrm{T}}}{\left\| \begin{bmatrix} -u' & -v' & w_0 - \Delta w/2 \end{bmatrix}^{\mathrm{T}} \right\|^3} dv' du' \\
& \qquad + \int_{-\Delta u/2}^{\Delta u/2} \int_{v_{\min,n}}^{v_{\max,n}} \frac{\begin{bmatrix} -u' & -v' & w_0 + \Delta w/2 \end{bmatrix}^{\mathrm{T}}}{\left\| \begin{bmatrix} -u' & -v' & w_0 + \Delta w/2 \end{bmatrix}^{\mathrm{T}} \right\|^3} dv' du' \\
& = \quad M_{\mathrm{w}} \boldsymbol{N}_{\mathrm{w}}. \tag{A.6}
\end{aligned}
$$

Using the results from (A.4-A.6), (A.3) can be written as

$$
\boldsymbol{H}_{\mathrm{ms}}(\boldsymbol{w}_0) = M_{\mathrm{u}} \boldsymbol{N}_{\mathrm{u}} + M_{\mathrm{v}} \boldsymbol{N}_{\mathrm{v}} + M_{\mathrm{w}} \boldsymbol{N}_{\mathrm{w}}. \tag{A.7}
$$

Despite writing the geometry dependent parts $\boldsymbol{N}_{\mathrm{u}}$, $\boldsymbol{N}_{\mathrm{v}}$ and $\boldsymbol{N}_{\mathrm{w}}$, as vectors, numerical examination shows that they can be approximated with confidence as scalars. To conclude, $\boldsymbol{H}_{\mathrm{ms}}$ is approximated as

$$
\boldsymbol{H}_{\mathrm{ms}}(\boldsymbol{w}_0) = \boldsymbol{N}\boldsymbol{M} = \begin{bmatrix} N_{\mathrm{u}} & 0 & 0 \\ 0 & N_{\mathrm{v}} & 0 \\ 0 & 0 & N_{\mathrm{w}} \end{bmatrix} \boldsymbol{M}. \tag{A.8}
$$